Parameterization of Cloud Microphysics Based on the Prediction of Bulk Ice Particle Properties. Part I: Scheme Description and Idealized Tests

HUGH MORRISON

National Center for Atmospheric Research, Boulder, Colorado*

JASON A. MILBRANDT

Atmospheric Numerical Prediction Research, Environment Canada, Dorval, Quebec, Canada

(Manuscript received 20 March 2014, in final form 3 August 2014)

ABSTRACT

A method for the parameterization of ice-phase microphysics is proposed and used to develop a new bulk microphysics scheme. All ice-phase particles are represented by several physical properties that evolve freely in time and space. The scheme prognoses four ice mixing ratio variables, total mass, rime mass, rime volume, and number, allowing 4 degrees of freedom for representing the particle properties using a single category. This approach represents a significant departure from traditional microphysics schemes in which ice-phase hydrometeors are partitioned into various predefined categories (e.g., cloud ice, snow, and graupel) with prescribed characteristics. The liquid-phase component of the new scheme uses a standard two-moment, two-category approach.

The proposed method and a complete description of the new predicted particle properties (P3) scheme are provided. Results from idealized model simulations of a two-dimensional squall line are presented that illustrate overall behavior of the scheme. Despite its use of a single ice-phase category, the scheme simulates a realistically wide range of particle characteristics in different regions of the squall line, consistent with observed ice particles in real squall lines. Sensitivity tests show that both the prediction of the rime mass fraction and the rime density are important for the simulation of the squall-line structure and precipitation.

1. Introduction

Proper representation of cloud microphysical and precipitation processes is critical for the simulation of weather and climate in atmospheric models. Despite decades of advancement, microphysics parameterization schemes still contain many uncertainties. This is due to an incomplete understanding of the important physical processes as well as the inherent complexity of hydrometeors in the real atmosphere. To represent the range of particles and their physical properties within the constraints of limited computational resources, current microphysics schemes use various hydrometeor categories defined by prescribed physical characteristics (e.g., shape, bulk density, terminal fall speeds, etc.) that broadly describe a given "typical" particle type. The relative simplicity of this approach has been successful in some aspects of parameterizing microphysics and problematic for others.

For liquid-phase microphysics in bulk schemes, the approach of separating drops into two categories,[1] defined essentially by size ranges, has worked reasonably well to model the onset of precipitation in warm clouds (Kessler 1969). This is because liquid drops are well represented by spheres with a density of liquid water ($\sim$1000 kg m^{-3}) up to sizes of several mm. There is also a clear separation of physical processes, with droplets

---

*The National Center for Atmospheric Research is sponsored by the National Science Foundation.

Corresponding author address: Hugh Morrison, National Center for Atmospheric Research, 3090 Center Green Drive, Boulder, CO 80301.
E-mail: morrison@ucar.edu

DOI: 10.1175/JAS-D-14-0065.1

[1] A bulk scheme with a single category of liquid has been proposed (Kogan and Belochitski 2012). This approach necessitates the inclusion of several additional prognostic moments to capture the nonlinear growth processes.

smaller than approximately 50–100 μm in diameter (generally referred to as ''cloud'' in bulk schemes) growing mainly by vapor diffusion and larger drops (''rain'') growing primarily by collision–coalescence. Separate categories for cloud and rain allow bulk schemes to simulate the rapid nonlinear growth of rain once embryo drops form by collision–coalescence. Two-moment bulk schemes do a remarkably good job in reproducing the evolution of unimodal spectrum of cloud droplet into a bimodal spectrum due to collection and coalescence as simulated by detailed bin-resolving models (Berry and Reinhardt 1974; Ziegler 1985; Cohard and Pinty 2000; Morrison and Grabowski 2007).

In contrast, the parameterization of ice-phase microphysics is more challenging and the use of predefined categories is inherently problematic. Unlike liquid drops, ice particles have a wide range of densities and complex shapes that affect their growth and decay processes. Moreover, they can grow by different processes (vapor diffusion, aggregation, riming) across a wide range of sizes. Partitioning ice-phase particles into a limited number of categories with specified shape, density, and other physical characteristics is a highly simplified representation of nature and necessitates the conversion of particles between categories, which is inherently artificial and often done without a strong theoretical or empirical basis. This approach is used in both spectral (bin) schemes (e.g., Reisin et al. 1996; Geresdi 1998; Khain et al. 2004; Lebo and Seinfeld 2011) and bulk schemes (e.g., Koenig and Murray 1976; Rutledge and Hobbs 1983; Lin et al. 1983; Ferrier 1994; Morrison et al. 2005; Milbrandt and Yau 2005b; Thompson et al. 2008). There is a large sensitivity of model simulations to how ice is partitioned into categories, and changes in thresholds or rates for conversion between ice species can lead to substantial differences in simulations (e.g., Colle et al. 2005; Morrison and Grabowski 2008a, hereafter MG08). Moreover, parameter settings for a given category, such as particle densities and fall speeds, are uncertain and simulations can exhibit considerable sensitivity to settings for these parameters (e.g., Gilmore et al. 2004; McFarquhar et al. 2006). For example, representing rimed ice with hail-like versus graupel-like characteristics can have large impacts on storm structure and precipitation associated with deep convection (e.g., McCumber et al. 1991; Gilmore et al. 2004; Cohen and McCaul 2006; Morrison and Milbrandt 2011; Bryan and Morrison 2012; Van Weverberg 2013; Adams-Selin et al. 2013).

There has been a general trend in the development of microphysics schemes to try and address these deficiencies by adding complexity to the representation of the ice phase, either by increasing the number of categories or adding more prognostic variables to existing categories. Earlier bulk schemes that included frozen hydrometeors used two categories—small ''cloud ice'' and larger, faster-falling ''snow'' (e.g., Rutledge and Hobbs 1983)—with conversion from one to the other based on an analogy of conversion from cloud liquid to rain. Walko et al. (1995) extended this approach by including cloud ice and snow and adding a separate category for crystal aggregates. To increase further the range of possible fall speeds, a rimed ice category (''graupel'' or ''hail'') was added (Lin et al. 1983; Rutledge and Hobbs 1984). In a few more recent schemes there is a user-specified switch allowing the rimed ice category to represent either fast-falling hail or slower-falling graupel (Morrison et al. 2009; Lang et al. 2011). To allow for both slower- and faster-falling rimed ice, other schemes have included separate categories for graupel and hail (e.g., Ferrier 1994; Milbrandt and Yau 2005b; Mansell et al. 2010). Straka and Mansell (2005) used three separate graupel/hail categories to track particles that originated from different processes.

With the exception of Koenig and Murray (1976), all earlier bulk schemes used only one prognostic variable per category—the mass mixing ratio—thus having a single degree of freedom to represent the size distribution. Two-moment schemes, where the mass and number mixing ratios are prognosed independently, were then developed (e.g., Ziegler 1985; Ferrier 1994; Seifert and Beheng 2001; Meyers et al. 1997; Morrison et al. 2005; Milbrandt and Yau 2005a; Philips et al. 2007; Lim and Hong 2010). The simulation of microphysical processes and sedimentation for a given category is generally improved with the two-moment approach (Ferrier 1994; Milbrandt and McTaggart-Cowan 2010; Dawson et al. 2010). A three-moment scheme was introduced by Milbrandt and Yau (2005a,b) whereby the inclusion of a third prognostic moment (reflectivity) allows for the prediction of the dispersion of the size spectrum, overcoming some of the limitations in two-moment schemes (in particular excessive size sorting due to sedimentation). To broaden further the range of validity for a given ice-phase category, recent work has added yet more complexity. For example, Connolly et al. (2006) relaxed the assumption of a fixed density for graupel by adding a prognostic variable for the bulk volume mixing ratio, with different graupel densities arising from different growth processes. This approach was advanced by Mansell et al. (2010) and Milbrandt and Morrison (2013) by using the predicted graupel density to include physically consistent fall speed calculations as well as empirical changes to the rime density. However, while the added complexity of these approaches allows for the representation of a wider range of particle characteristics, inherently artificial conversion processes are still required with the use of separate predefined ice categories. Furthermore, greater complexity by increasing the number of categories means an increase in the number of uncertain conversion processes and parameters, which may inherently limit improvements that one might expect with the increased complexity.

An alternative approach that evolves particle properties in time and space instead of separating ice into different predefined categories was first proposed in the bin microphysics scheme of Hashino and Tripoli (2007). MG08 developed a bulk scheme that separately prognoses ice mass mixing ratios grown by riming and vapor deposition to improve the treatment of the transition between unrimed snow, rimed snow, and graupel. Harrington et al. (2013a,b) and Sulia et al. (2013) developed a bulk scheme that predicts particle habit evolution by including the crystal a- and c-axis mixing ratios as prognostic variables, thereby allowing for prediction of crystal axis ratio from vapor depositional growth. Other schemes have used a diagnostic approach to include variability in ice particle properties (Lin and Colle 2011; Eta Ferrier scheme). Lin and Colle (2011) included separate categories for cloud and precipitating ice and diagnosed the degree of riming and ice particle properties (mass–size and fall speed–size relationships) for precipitating ice as a function of the ratio of the riming to the riming plus vapor deposition growth rates. Such a diagnostic approach is computationally efficient because it does not require additional prognostic variables, but the disadvantage is that particle properties are calculated locally and are not tracked in time and space.

These efforts represent a broader shift in the representation of ice microphysics by emphasizing the prediction of particle properties rather than the separation of ice into different predefined categories. In this study, the approach is generalized and a method is proposed to predict several bulk physical properties of ice particles, which can evolve through the full range of growth and decay processes. The implementation described in this paper uses a single ice-phase category. The proposed approach thus completely eliminates the need for artificial conversion between ice categories. This forms the basis for a conceptually new bulk microphysics scheme. This study introduces the proposed approach and new scheme and demonstrates its overall performance. A detailed description of the method and the scheme are provided in this paper along with idealized simulations to illustrate its behavior and sensitivity to key parameters. In Morrison et al. (2015, hereafter Part II), results from kilometer-scale simulations using the new scheme for two real cases—deep convection and orographically enhanced frontal precipitation—are compared to those using existing bulk schemes that employ the traditional predefined ice-category approach.

The remainder of the article is organized as follows. Section 2 provides a description of the method and the new scheme. Section 3 presents simulations of an idealized two-dimensional (2D) squall line that illustrate the overall behavior of the scheme. A summary and conclusions are given in section 4.

2. Scheme description

a. Overview

A new bulk scheme using the proposed approach has been developed, which we refer to as the predicted particle properties (P3) scheme. To represent the evolution of various physical properties in space and time, the scheme includes a single ice-phase category with four prognostic mixing ratio variables: the total ice mass q_i, ice number N_i, the ice mass from rime growth q_{rim}, and the bulk rime volume B_{rim}. These are chosen as the conserved prognostic variables because together they are able to track particle evolution through all the important mechanisms of ice growth, including vapor deposition, aggregation, and riming (dry and wet growth). From this choice of prognostic variables, several important predicted properties are derived, including the rime mass fraction, bulk density, and mean particle size. Here we distinguish between "prognostic" variables, which are conserved and include dynamical tendencies from advection and subgrid-scale mixing and microphysical tendencies (growth/decay processes and sedimentation), and "predicted" quantities, which are derived directly from the prognostic variables and hence vary locally in time and space. The liquid-phase component of the scheme is summarized in appendix A.

The conservation equation for any prognostic microphysical variable χ has the form

$$\frac{\partial \chi}{\partial t} = -\mathbf{u} \cdot \nabla \chi + \frac{1}{\rho}\frac{\partial(\rho V_{\chi}\chi)}{\partial z} + S_{\chi} + \Delta^{*}(\chi), \qquad (1)$$

where $\chi \in q_c, q_r, N_c, N_r, q_i, q_{\text{rim}}, B_{\text{rim}}, N_i$, t is time, ρ is the air density, $\mathbf{u}$ is the 3D wind vector, z is height, $V\chi$ is the appropriately weighted fall speed for quantity χ, $S\chi$ is the source/sink term and includes various microphysical processes, and $\Delta^{*}(\chi)$ is the subgrid-scale mixing operator (all symbols for variables and parameters used in the paper are defined in Table 1). Microphysical process rates that determine $S\chi$ are described in appendix B. The process rates depend on various moments

TABLE 1. List of symbols for variables and parameters.

Symbol	Description	Value
μ	Shape parameter	
λ	Slope parameter	
Γ_i	Psychrometric correction to vapor deposition/sublimation for ice	
Γ_l	Psychrometric correction to vapor deposition/sublimation for liquid	
γ_r	Rain number evaporation factor	0.5
τ_{sb}	Relaxation time scale for rain drop breakup	$10\ \mathrm{s}$
Δt	Model time step	
α	Coefficient in *m–D* relation for generic ice	
α_{va}	Coefficient in *m–D* relation for large, unrimed ice	
α_r	Coefficient in *m–D* relation for partially rimed ice	
β	Exponent in *m–D* relation for generic ice	
β_x	Exponent in *m–D* relation for hydrometeor *x*	
β_{va}	Exponent in *m–D* relation for large, unrimed ice	
β_r	Exponent in *m–D* relation for partially rimed ice	
δ	Absolute supersaturation with respect to liquid	
Δ^*	Subgrid-scale mixing operator	
χ	Generic prognostic microphysical variable	
ρ	Air density	
ρ_0	Reference air density for fall speed calculations	
ρ^*	Density of rime during wet growth and freezing	$900\ \mathrm{kg\,m^{-3}}$
ρ_d	Density of unrimed ice mass	
ρ_g	Density of total (deposition plus rime) ice mass for graupel	
ρ_i	Bulk density of solid ice	$917\ \mathrm{kg\,m^{-3}}$
ρ_p	Mass-weighted mean particle density	
ρ_r	Predicted density of rimed ice mass	
ρ'_r	Instantaneous density of collected rime	
ρ_w	Density of liquid water	$1000\ \mathrm{kg\,m^{-3}}$
τ	Supersaturation relaxation time scale for the sum of cloud droplets, rain, and ice	
τ_x	Supersaturation relaxation time scales for $x = c, r, i$	
A	Projected particle area	
A_c	Parameter in supersaturation equation	
a_1	Coefficient in fall speed–diameter relation for ice	
b_1	Exponent in fall speed–diameter relation for ice	
c_p	Specific heat of air at constant pressure	$1005\ \mathrm{J\,kg^{-1}}$
D	Maximum particle dimension	
D_{cr}	Size of equal mass for graupel and partially rimed ice	
D_{gr}	Size of equal mass for graupel and unrimed ice	
D_m	Mass-weighted mean particle size	
D_{mr}	Scaled mean rain diameter	
D_n	Number-weighted mean particle diameter	
D_{rt}	Critical diameter for raindrop breakup	
D_{sb}	Relaxation diameter for raindrop breakup	$2.4 \times 10^{-3}\ \mathrm{m}$
D_{th}	Critical size separating spherical/nonspherical ice	
E_{cr}	Efficiency of rain self-collection	
e_s	Saturation vapor pressure with respect to liquid	
F_r	Bulk rime mass fraction	
g	Acceleration of gravity	$9.81\ \mathrm{m\,s^{-2}}$
L_s	Latent heat of sublimation	
L_v	Latent heat of vaporization	
m_r	Mass of a partially rimed ice particle	
m_{va}	Particle mass grown by vapor diffusion/aggregation	
m_g	Mass of a graupel particle	
$N'(D)$	Number concentration for D to $D + dD$	
N_0	Intercept parameter	
N_c	Total number mixing ratio for cloud droplets	
N_i	Total number mixing ratio for ice	
N_r	Total number mixing ratio for rain	
p	Air pressure	
q	Water vapor mixing ratio	
q_c	Mass mixing ratio for cloud droplets	
q_i	Total (deposition plus rime) mass mixing ratio for ice	
q_r	Mass mixing ratio for rain	
q_{rim}	Rime mass mixing ratio for ice	
q_{si}	Saturation mixing ratio with respect to ice	
q_{sl}	Saturation mixing ratio with respect to liquid	
R_e	Reynolds number	
S_i	Supersaturation with respect to ice	
S_x	Microphysical source term for category *x*	
t	Time	
T	Temperature	
u	3D wind vector	
V	Terminal fall speed	
V_m	Mass-weighted terminal fall speed	
V_N	Number-weighted fall speed	
w	Vertical air velocity	
X	Best (Davies) number	
z	Height above ground	
Z	Equivalent radar reflectivity	

of the particle size distributions, represented by a three-parameter gamma distribution of the form

$$N'(D) = N_0 D^{\mu} e^{-\lambda D}, \tag{2}$$

where D is the maximum particle dimension and N_0, λ, and μ are the intercept, slope, and shape parameters, respectively. For ice, μ follows from the in situ observations of Heymsfield (2003) based on particle size distribution (PSD) fits to tropical and midlatitude particle ensembles in ice clouds:

$$\mu = 0.001\,91\lambda^{0.8} - 2, \tag{3}$$

where λ has units of per meter in this formulation. For simplicity and following MG08, μ is limited to $0 < \mu < 6$, although Heymsfield (2003) shows negative values of μ for $\lambda < \sim 7000\,\mathrm{m}^{-1}$. Based on this formulation nonzero μ only occur for rather small mean particle size ($1/\lambda < \sim 0.17$ mm).

The size distribution parameters N_0 and λ are related to the prognostic number mixing ratio N and mass mixing ratio q by

$$N = \int_0^{\infty} N'(D)\,dD = \int_0^{\infty} N_0 D^{\mu} e^{-\lambda D}\,dD \quad \text{and} \tag{4}$$

$$q = \int_0^{\infty} m(D) N'(D)\,dD = \int_0^{\infty} m(D) N_0 D^{\mu} e^{-\lambda D}\,dD, \tag{5}$$

where $m(D)$ is the particle mass as a function of D and $N'(D)$ is given by (2).

Although the current version of the P3 scheme has one ice-phase category, it is a "free category" in that, because of the evolution of its predicted properties, it can represent any type of ice particle. This is in stark contrast with "prescribed categories" in traditional schemes, whose evolution is intrinsically constrained. However, the one-category P3 scheme has the inherent limitation that it cannot simulate populations of particles with different bulk properties at the same point in time and space. Thus, attempting to capture a mixture of particles with substantially different bulk characteristics can lead to problems under certain conditions. For example, in deep, strong updrafts that loft both supercooled liquid water and large graupel to the homogeneous freezing level, rapid droplet freezing and production of a high small ice particle concentration might smear out characteristics of the large graupel. A similar situation occurs for Hallett and Mossop (1974) rime splintering. To minimize this problem, the current version neglects ice multiplication by rime splintering. Despite the limitation of using a single category, it produces results that compare well with observations relative to other bulk microphysics schemes for the real cases tested in Part II. In future development we plan to implement a multiple-free-category approach in P3 to address this limitation, as described in section 4. The multiple-free-category version will also be compared with the single-category version to test systematically the effects of this limitation.

b. *Particle mass, projected area, and fall speed*

Integrating (4) and (5) over the PSD and solving for N_0 and λ requires specification of the m–D relationship over the size distribution. For cloud droplets and rain, this is given simply by the relationship for spherical liquid drops: $\pi\rho_w D^3/6$. For ice particles, the m–D relationship varies in time and space and over the range of particle sizes and is calculated from the predicted properties derived from the prognostic quantities. The approach is broadly similar to that of MG08 but with important distinctions as noted below.

Small ice particles are approximated as ice spheres with an effective density equal to that of bulk ice $\rho_i = 917\,\mathrm{kg\,m^{-3}}$. It follows that the m–D relationship for small ice is

$$m = \frac{\pi}{6}\rho_i D^3. \tag{6}$$

Larger ice particles, regardless of the mode of growth, are generally nonspherical and have an effective density less than that of an ice sphere of the same D (for nonspherical ice, D is defined as the maximum particle length or dimension). For larger unrimed crystals grown by vapor diffusion and/or aggregation (i.e., when $q_i > 0$ and $q_{\mathrm{rim}} = 0$), the m–D relationship is expressed as a power law:

$$m_{\mathrm{va}} = \alpha_{\mathrm{va}} D^{\beta_{\mathrm{va}}}. \tag{7}$$

The parameters from Brown and Francis (1995) are used for α_{va} and β_{va}, derived from measurements in midlatitude cirrus. Other empirically or theoretically derived values for α_{va} and β_{va} could be used. There is some sensitivity of simulations to the choice of α_{va} and β_{va}; detailed discussion is beyond the scope of this paper but such tests are described in MG08 for their scheme. Changes in particle density associated with vapor diffusion and aggregation are implicitly included in (7) because the density decreases with increasing D (since $\beta_{\mathrm{va}} < 3$). The critical size separating spherical ice from unrimed nonspherical ice is found by extrapolating the m–D relationship in (7) down to the size that it equals the mass of an ice sphere for the same D following Heymsfield et al. (2007). This critical size D_{th} is given by

$$D_{\mathrm{th}} = \left(\frac{\pi\rho_i}{6\alpha_{\mathrm{va}}}\right)^{1/(\beta_{\mathrm{va}}-3)}. \quad (8)$$

Representation of the m–D relationship is considerably more complicated for rimed particles (i.e., when $q_{\mathrm{rim}} > 0$). Following MG08 and based on the conceptual model of riming introduced by Heymsfield (1982), it is assumed that rime accumulates in the crystal interstices as the particle undergoes riming, increasing m but not D. Once the particle is "filled in" with rime, the particle is considered to be graupel[2] and further growth increases both m and D. [Note that the scheme distinguishes between wet and dry riming growth (see appendices B and C).] It is also assumed that prior to in-filling of the crystal interstices with rime, the rime mass fraction of an individual particle F_r is equal to the bulk rime mass fraction given by $F_r = q_{\mathrm{rim}}/q_i$. It follows that

$$F_r = \frac{m_r - m_{\mathrm{va}}}{m_r}, \quad (9)$$

where m_{va} is the portion of the crystal mass grown by vapor diffusion and aggregation and m_r is the total particle mass of a partially rimed crystal. It is assumed that the m–D relationship for partially rimed crystals also follows a power-law relationship:

$$m_r = \alpha_r D^{\beta_r}. \quad (10)$$

Since D is not affected by riming up to the point of complete rime in-filling based on the conceptual model of riming discussed above, it follows that m_{va} is given by (7). Combining (7), (9), and (10) and rearranging terms yields

$$\alpha_r D^{\beta_r} = \frac{\alpha_{\mathrm{va}}}{(1-F_r)} D^{\beta_{\mathrm{va}}}. \quad (11)$$

Since we assume constant F_r with D and (11) holds true for arbitrary D, this uniquely implies that $\alpha_r = \alpha_{\mathrm{va}}/(1 - F_r)$ and $\beta_r = \beta_{\mathrm{va}}$. It follows that the m–D relationship for partially rimed crystals is

$$m_r = \left(\frac{1}{1-F_r}\right)\alpha_{\mathrm{va}} D^{\beta_{\mathrm{va}}}. \quad (12)$$

There is observational evidence supporting the assumption of constant β during riming (which follows logically from the conceptual model of rime in-filling and the assumption that F_r is constant with D). Rogers (1974) found the same β in the m–D relationship for rimed and unrimed snowflakes, with α about 4 times larger for rimed snow. Similarly, riming appears to have little effect on β for hexagonal columns, with a value 1.8 for both unrimed and rimed crystals [see Table 1 and section 4d of Mitchell et al. (1990)]. More recent analysis has also shown that the β parameter varies much less than α for rimed and unrimed crystals of the same underlying habit. Mitchell and Erfani (2014) show α of 0.001 263 and 0.001 988 for unrimed and heavily rimed dendrites, respectively, with β of 1.912 and 1.784. If the size interval corresponding with the largest unrimed dendrites is excluded, then β becomes 1.786, almost the exactly the same as for heavily rimed dendrites.

The previous derivation for partially rimed crystals is valid up to the point of complete in-filling by rime. Complete in-filling occurs when the mass of a partially rimed crystal m_r equals the mass of a graupel particle m_g for the same D. In contrast to the approach of MG08, which assumed an empirically derived m–D relationship for graupel, here graupel particles are assumed to be spherical with an effective density ρ_g that is predicted and varies locally in time and space. Thus, the m–D relationship for graupel is

$$m_g = \frac{\pi}{6}\rho_g D^3. \quad (13)$$

The critical size for complete in-filling with rime D_{cr} is found by equating the masses of partially rimed crystals and graupel particles (i.e., setting $m_r = m_g$). Using the m–D relationships for m_r and m_g following (12) and (13), respectively, and rearranging terms to solve for $D = D_{\mathrm{cr}}$ yields

$$D_{\mathrm{cr}} = \left[\left(\frac{1}{1-F_r}\right)\frac{6\alpha_{\mathrm{va}}}{\pi\rho_g}\right]^{1/(3-\beta_{\mathrm{va}})}. \quad (14)$$

The m–D relationship for graupel given by (13) applies to a limited size range. Extrapolation of this relationship to smaller sizes leads to a bulk density of graupel that is less than that of unrimed ice. To avoid this inconsistency we follow the approach of MG08 and define a third critical size D_{gr} that represents the size where the masses of graupel and unrimed ice are equal. Particles smaller than D_{gr} are assumed to have an m–D relationship corresponding to unrimed ice, even though they may be rimed, to avoid low bulk densities for small particles and discontinuities in the particle mass as a function of D across the PSD. Particles with sizes $D_{\mathrm{th}} < D < D_{\mathrm{gr}}$ are referred to as "dense nonspherical ice." The value of D_{gr} is found by setting $m_g = m_{\mathrm{va}}$ and solving for $D = D_{\mathrm{gr}}$:

---

[2] For simplicity, we refer to all dense rimed ice as graupel unless otherwise noted, even though large (>5 mm) rimed particles and/or high-density particles that have undergone wet growth are traditionally referred to as hail.

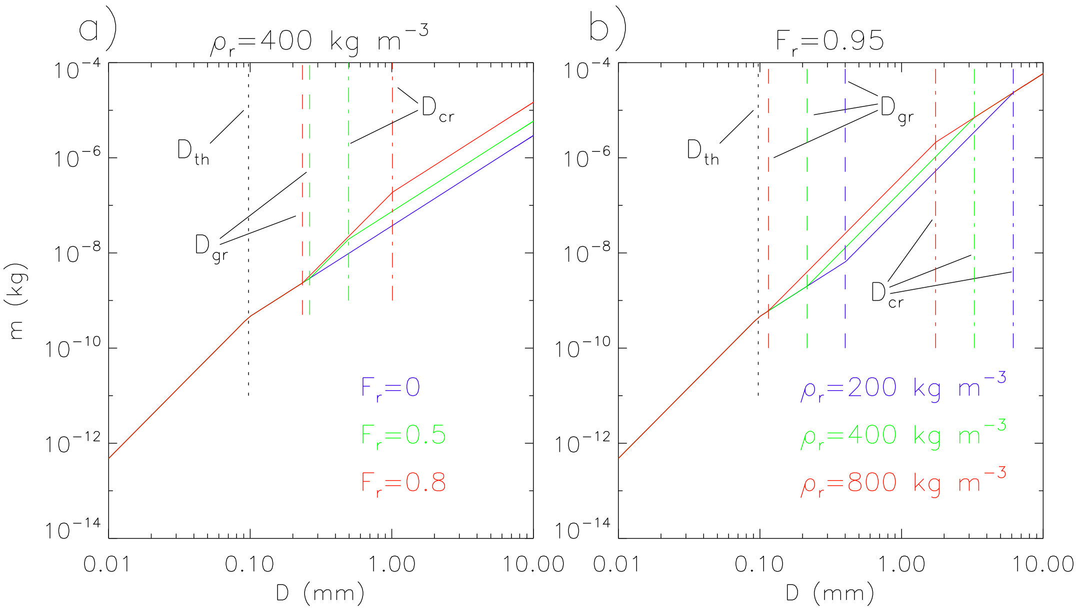

FIG. 1. Examples of the ice particle m–D relationship across the range of particle sizes (solid colored lines): (a) relationship for three different values of F_r (0, 0.5, 0.8) assuming constant $\rho_r = 400\,\mathrm{kg\,m^{-3}}$ and (b) relationship for three different values of ρ_r (200, 400, 800 kg m^{-3}) assuming constant $F_r = 0.95$. Vertical lines show the critical sizes separating small spherical ice from dense nonspherical (or unrimed ice) ice (D_{th}; dotted black lines), dense nonspherical ice from graupel (D_{gr}; colored dashed lines), and graupel from partially rimed crystals (D_{cr}; colored dotted–dashed lines). The colors for D_{gr} and D_{cr} correspond to the given F_r and ρ_r indicated in the plots (D_{th} is independent of F_r and ρ_r).

$$D_{\mathrm{gr}} = \left(\frac{6\alpha_{\mathrm{va}}}{\pi\rho_g}\right)^{1/(3-\beta_{\mathrm{va}})}. \tag{15}$$

Thus, D_{gr} depends on the mass–size relation for unrimed ice (α_{va} and β_{va}) as well as ρ_g. Here ρ_g depends on the history of rime growth (including the effects of densification due to wet growth) and the underlying (unrimed) habit of particles that form graupel. The value of ρ_g is found by calculating an F_r-weighted average of the predicted rime density, $\rho_r = q_{\mathrm{rim}}/B_{\mathrm{rim}}$, combined with the density of the unrimed part of the particle ρ_d:

$$\rho_g = \rho_r F_r + (1 - F_r)\rho_d, \tag{16}$$

where ρ_d is found by a mass-weighted averaging of the unrimed particle density between sizes D_{gr} and D_{cr}, giving

$$\rho_d = \frac{6\alpha_{\mathrm{va}}(D_{\mathrm{cr}}^{\beta_{\mathrm{va}}-2} - D_{\mathrm{gr}}^{\beta_{\mathrm{va}}-2})}{\pi(\beta_{\mathrm{va}} - 2)(D_{\mathrm{cr}} - D_{\mathrm{gr}})}. \tag{17}$$

For nonspherical particles, particle density is defined here as the particle mass divided by the volume of a sphere with the same D. Equations (14)–(17) form a closed set of equations for ρ_d, ρ_g, D_{cr}, and D_{gr} that is solved by iteration.

Figure 1 illustrates how the PSD is partitioned into different regions following this approach. If ρ_r is held constant, increasing F$_r$ increases the density of partially rimed crystals (i.e., larger mass for a given D) in the region of the PSD with $D > D_{\mathrm{cr}}$ (Fig. 1a). Increasing F_r also leads to an increase in D_{cr}, the critical size separating particles that have filled in with rime (i.e., graupel) with partially rimed crystals, following (14). Because of the interdependence of D_{cr}, D_{gr}, F_r, and ρ_r following (14)–(17), increasing F_r also produces a small increase in ρ_g and a small decrease in D_{gr}. For example, increasing F_r from 0.5 to 0.8 leads to relative changes in ρ_g and D_{gr} of about 10%. If instead F_r is held constant, increasing ρ_r leads to an increase in the density of graupel—that is, particles in the region of the PSD between D_{gr} and D_{cr}, as well as an increase in the critical size D_{gr} (Fig. 1b), as long as $F_r > 0$. On the other hand, D_{cr} decreases with increasing ρ_r since higher rime density means that more rime mass can accumulate on partially rimed crystals before the total particle mass is equal to that of a graupel particle for a given D (in other words, more rime mass can accumulate before partially rimed crystals become filled in with rime). The mass of particles with D greater than about 1 mm is more sensitive to F_r than ρ_r overall. This has implications for bulk parameters such as the mass-weighted fall speed as described below.

Another important hydrometeor property is the projected area $A(D)$ since this is needed to calculate fall speeds and effective radii. For cloud droplets, rain, dense ice spheres ($D < D_{\mathrm{th}}$), and graupel ($D_{\mathrm{gr}} < D < D_{\mathrm{cr}}$), the particle projected area is simply given by the A–D relationship for spheres, $A = \pi D^2/4$. For dense nonspherical ice and unrimed nonspherical ice, the A–D relationship is empirically derived from ice particle observations. Here we use parameters for aggregates of side planes, bullets, and columns and assemblages of planar polycrystals from Mitchell (1996) and references therein. Other empirical A–D relationships could be employed, but it is important that the relationship is consistent with the m–D relationship employed, as otherwise unreasonable values of fall speed may occur since this depends on m/A. Such consistency is described theoretically by the fractal approach of Schmitt and Heymsfield (2010). Since the conceptual model of riming described above does not provide information on the evolution of projected area for partially rimed crystals, for simplicity a simple linear weighting is assumed between the value for graupel (i.e., spheres) and unrimed ice as a function of F_r following MG08.

It is critical to link fall speed to the m–D and A–D relationships because particle densities vary in time and space. In most bulk microphysics schemes, particle densities are fixed and ice particle fall speed is simply given as a power law of D without explicit dependence on density. Such an approach leads to an incorrect dependence of fall speed on density if the density is modified; fall speed decreases when the particle density is increased since this leads to a decrease in the mean particle size. In the proposed approach, the terminal fall speed of ice follows a power-law relationship $V = a_1 D^{b_1}$. The coefficients a_1 and b_1 are derived following Mitchell and Heymsfield (2005) based on the R_e–X relationship, where R_e is the particle Reynolds number and X is the Best (Davies) number (related to the ratio of the particle mass to its projected area). This approach follows Khvorostyanov and Curry (2002) to calculate smooth a_1 and b_1 as a function of D but modified to include surface roughness coefficients appropriate for ice particles. The particle mass and projected area are found from the m–D and A–D relationships described above and, hence, include an explicit dependence on particle density. Since F_r and ρ_r are assumed to be independent of D, the same mass-weighted terminal fall speeds are applied to q_i, q_{rim}, and B_{rim}, while the number-weighted terminal fall speed is applied to N_i as described earlier.

The air density modification of particle fall speeds for rain and ice follows Heymsfield et al. (2007), which gives a multiplicative factor of $(\rho_0/\rho)^{0.54}$ for the fall speed, where ρ_0 is a reference air density. Note this correction is not applied to cloud droplets since Stokes' law implicitly includes a dependence on environmental conditions through the dynamic viscosity of air.

The size distribution parameters N_0 and λ are derived from (4) and (5). For cloud droplets and rain, the integrals in (4) and (5) can be calculated analytically using Euler gamma functions since the parameters in the m–D relationship in (5) are constant across the PSD. Hence, analytic expressions can be derived for N_0 and λ [e.g., see (2) and (3) in Morrison (2012)]. For ice, however, the integral in (5) involves incomplete gamma functions because the m–D relationship varies across different regions of the PSD. Thus, N_0 and λ cannot be derived analytically and are instead solved by iteration. Since this is computationally expensive, a lookup table approach is employed to make the scheme computationally efficient. Values of N_0, λ, and moments of the PSD relevant to calculation of the microphysical process rates and parameters for ice are precalculated and stored in a lookup table as a function of q_i, N_i, F_r, and ρ_r.

Figure 2 illustrates the mass-weighted ice fall speed V_m as a function of F_r and ρ_r for a given q_i/N_i corresponding to small, medium, and large values of mass-weighted mean particle size D_m (note that D_m is not constant for a given q_i/N_i because it changes with F_r and ρ_r). For small D_m there is little sensitivity of V_m to either F_r or ρ_r (Fig. 2a). This is because as D_m shifts to small sizes the size distribution becomes dominated by small spherical ice, which has a bulk density of solid ice regardless of F_r or ρ_r. Interestingly, larger ρ_r and F_r actually produce slightly smaller V_m because this leads to smaller D_m for a given q_i/N_i. The picture differs for larger D_m, with much greater sensitivity to ρ_r and F_r (Figs. 2b,c). As expected, V_m increases with an increase in either ρ_r or F_r. However, there is somewhat greater sensitivity to F_r than ρ_r, which reflects greater sensitivity of the m–D relationship to F_r (see Fig. 1). Also shown in Figs. 2b and 2c are V_m calculated from empirical power-law V–D relationships for different ice particle types integrated over the PSD. While observed values of F_r and ρ_r have not been quantified as a function of particle type, it is reasonable to assume that F_r increases between rimed snow [rimed dendrites and aggregates of dendrites from Locatelli and Hobbs (1974)], graupel-like snow (Locatelli and Hobbs 1974), lump graupel (Locatelli and Hobbs 1974), and hail (Matson and Huggins 1980; Ferrier 1994). We also assume ρ_r is larger for hail ($\sim$900 kg m^{-3}) compared to the other particle types ($\sim$400 kg m^{-3}). The modeled V_m are 1.5–2 m s^{-1} for rimed snow (assuming $F_r \sim 0.2$ and $\rho_r \sim 400$ kg m^{-3}), 1.5–3 m s^{-1} for graupel-like snow and lump graupel

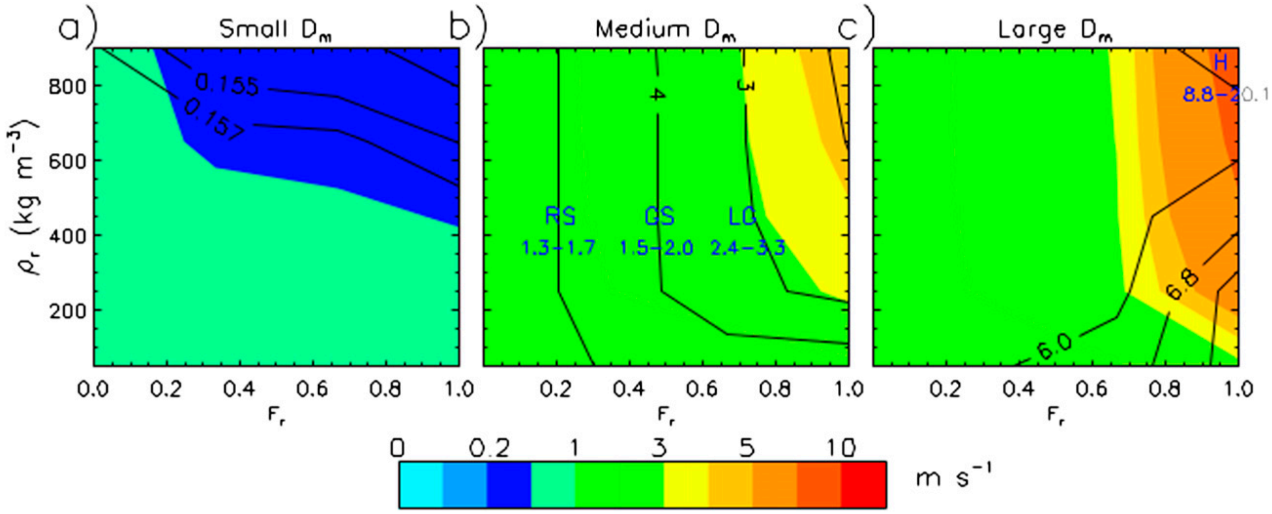

FIG. 2. Mass-weighted bulk ice fall speed as a function of F_r and ρ_r for (a) small D_m (~0.15–0.16 mm), (b) medium D_m (~2–5 mm), and (c) large D_m (~5–7 mm). Black contour lines represent D_m. Empirical values for rimed snow (RS), graupel-like snow (GS), lump graupel (LG), and hail (H) are shown in blue text in (b) and (c). Calculations are made for a temperature of −20°C and a pressure of 600 hPa.

(assuming $F_r \sim 0.5$–0.7 and $\rho_r \sim 400$ kg m^{-3}), and greater than 8 m s^{-1} for large hail (assuming $F_r \sim 1$ and $\rho_r \sim 900$ kg m^{-3}). These values are reasonably similar to the range of empirical V_m for a given ice particle type.

c. Numerical implementation

The scheme uses a time-split forward Euler solution similar to most other microphysics schemes. Within a time step, the scheme first calculates all of the microphysics source/sink processes in $S\chi$ following (B1)–(B8) (see appendix B) except homogeneous freezing of cloud water and rain. It then updates all prognostic state variables with these tendencies. These updated variables are used to calculate sedimentation, after which the scheme further updates the prognostic variables. Sedimentation is calculated using a simple first-order upwind method following several other microphysical schemes (e.g., Reisner et al. 1998; Thompson et al. 2008; Morrison et al. 2009) with substepping as needed for numerical stability based upon the Courant–Friedrichs–Levy criterion. Lastly, the scheme calculates homogeneous freezing of cloud water and rain and updates variables at the end of the microphysical calculations. Homogeneous freezing is calculated at the end of the microphysics time step to avoid the unphysical situation of having significant liquid water at temperatures colder than 233 K.

Conserved (extensive) quantities q_i, $q_{\rm rim}$, $B_{\rm rim}$, and N_i are included as the choice of prognostic variables. Two of the key properties predicted in the scheme, F_r and ρ_r, depend on the ratio of these prognostic variables: $F_r = q_{\rm rim}/q_i$ and $\rho_r = q_{\rm rim}/B_{\rm rim}$. This limits errors in the F_r and ρ_r fields that occur during advection and is one reason these particular prognostic variables are used. Despite limited error when coupled with transport, some drift may occur, which can lead to inconsistency between the mass, number, and volume mixing ratios, especially when the quantities are very small. To address this, λ is limited to a range of values, as is done in all multimoment bulk microphysics schemes. This is accomplished by limiting the number-weighted mean particle diameter, $D_N = (\mu + 1)/\lambda$, to $1 < D_N < 40\,\mu$m for cloud water and $2 < D_N < 2000\,\mu$m for ice. If D_N is outside of these bounds, then N is adjusted so that D_N lies within the specified range for each species. The predicted rime density ρ_r is also limited to values between 50 and 900 kg m^{-3}. If necessary, $B_{\rm rim}$ is adjusted to keep ρ_r within this specified range.

3. Idealized 2D squall-line simulations

a. Setup

This section describes a set of simulations that illustrate the behavior of the new scheme. We use the Weather Research and Forecasting (WRF) Model (Skamarock et al. 2008), version 3.4.1, which is a compressible, nonhydrostatic dynamical atmospheric model. The following tests use WRF in a 2D configuration similar to the standard idealized squall-line test case. Two-dimensional idealized tests are used here because the simplicity of this model setup allows us to clearly demonstrate behavior of the scheme. The focus here is on the microphysics; interactions between microphysics and dynamics are explored further in Part II.

The governing equations are solved using a time-split integration with a third-order Runge–Kutta scheme. Horizontal and vertical turbulent diffusion are calculated using a 1.5-order turbulence kinetic energy (TKE) scheme (Skamarock et al. 2008). Third- and fifth-order discretization schemes are used for vertical and horizontal advection, respectively, with limiters to ensure monotonicity (Wang et al. 2009). The upper and lower boundaries are free slip with zero vertical velocity. Surface fluxes are set to zero and radiative transfer is neglected for simplicity. A Rayleigh damper is applied to the upper 5 km with a damping coefficient of $0.003\,\mathrm{s}^{-1}$. The horizontal grid spacing is 1 km, with 80 vertical levels between the surface and model top. The time step is 5 s and the domain size is 500 km in the horizontal and 20 km in the vertical. Lateral boundary conditions are open. Radar reflectivity is calculated assuming Rayleigh scattering following the approach of Smith (1984) using the predicted size distribution and particle density parameters. A discussion of the uncertainties in using this approach is discussed in Smith (1984) and in Part II and references therein.

The model is initialized with the analytic sounding of Weisman and Klemp (1982, 1984). The initial vertical wind shear is $0.0048\,\mathrm{s}^{-1}$ applied between the surface and 2.5 km (meaning that horizontal wind changes $12\,\mathrm{m\,s}^{-1}$ between the surface and 2.5 km). Convection is initiated by adding a thermal with maximum perturbation potential temperature of 3 K centered at a height of 1.5 km and varying as the cosine squared to the perturbation edge. The thermal has a horizontal radius of 4 km and a vertical radius of 1.5 km. Model integrations are for 6 h.

b. Baseline results

Moist convection is triggered within the first few minutes of the simulation from the initial thermal. Ice is initiated after approximately 10 min, and precipitation reaches the surface after approximately 20 min. In its early stages the storm is nearly symmetric, but significant horizontal asymmetry develops over time in response to the environmental shear. After about 4 h the storm reaches a quasi-equilibrium mature phase with a well-defined leading edge of convection and trailing stratiform precipitation.

Storm evolution in the baseline (BASE) simulation (see Table 2) is illustrated by vertical cross-section plots. Figures 3 and 4 show prognostic microphysical quantities and key predicted particle properties, respectively, at 2 h. Figures 5 and 6 show these same quantities at 6 h. During the early, quasi-symmetric phase of the storm at 2 h, there is a 5–10-km-wide convective core of high radar reflectivity Z, with a peak Z at the lowest model level of 52.3 and 60.3 dBZ aloft (Fig. 4a). There are large amounts of cloud water and rain within and below the convective core (Figs. 3a,b). Ice condensate with mixing ratios exceeding $8\,\mathrm{g\,kg}^{-1}$ occur in the core, with the q_i, q_{rim}, and B_{rim} fields exhibiting a similar pattern (Figs. 3c–e). The value of N_i exhibits a sharp increase with height (Fig. 3f) owing to freezing of cloud droplets in the convective core and detrainment at upper levels as well as size sorting effects and aggregation. The convective core has values of F_r close to 1 (Fig. 4b) associated with large amounts of supercooled liquid water and hence large riming and drop freezing rates. It also has values of mean mass-weighted ice particle density ρ_p from about 300 to $600\,\mathrm{kg\,m}^{-3}$ (Fig. 4c). Here ρ_p is calculated as

$$\rho_p = \frac{\int_0^\infty (6\alpha^2/\pi) D^{2\beta-3+\mu} e^{-\lambda D}\, dD}{\int_0^\infty \alpha D^{\beta+\mu} e^{-\lambda D}\, dD}, \qquad (18)$$

where α and β are parameters of the power-law mass–size relationships that vary between the four regions of the PSD described in section 2c and shown in Fig. 1. The values of V_m reach 5–$8\,\mathrm{m\,s}^{-1}$ in the high-density core region (Fig. 4d). Also ρ_p increases with height outside of the convective core as a consequence of the decrease in D_m with height (Fig. 4e); ρ_p is close to the density of solid spherical ice ($\sim 900\,\mathrm{kg\,m}^{-3}$) near cloud top where $D_m < 0.1$ mm but is less than $100\,\mathrm{kg\,m}^{-3}$ lower in the anvil region outside of the convective core, where $D_m \sim$ 3–5 mm. Sensitivity tests show the sharp vertical gradient of D_m in the anvil region is partly a result of aggregation and size sorting, while other factors such as increased vapor depositional growth in the relatively warmer temperatures at lower altitudes also likely play a role. Fairly large mean particle sizes ($D_m \sim$ 3–4 mm, $\lambda \sim$ 8–$10\,\mathrm{cm}^{-1}$) occur above the melting level outside of the convective core and are consistent with aircraft observations of λ in deep precipitating stratiform cloud systems (Heymsfield et al. 2008).

By 6 h, the storm has developed significant horizontal asymmetry associated with the environmental shear (Figs. 5–6). There is a leading edge of high reflectivity (>45 dBZ) associated with intense convection near the cold pool edge and a large region of trailing stratiform

TABLE 2. List of idealized 2D squall-line microphysics tests.

BASE	Baseline version of the new P3 microphysics scheme
ρ400	As in BASE, except rime density ρ_r is set to $400\,\mathrm{kg\,m}^{-3}$
ρ900	As in ρ400, except $\rho_r = 900\,\mathrm{kg\,m}^{-3}$
FR0	As in BASE, except rime mass fraction F_r is set to 0
FR1ρ400	As in BASE, except $F_r = 1$ and $\rho_r = 400\,\mathrm{kg\,m}^{-3}$

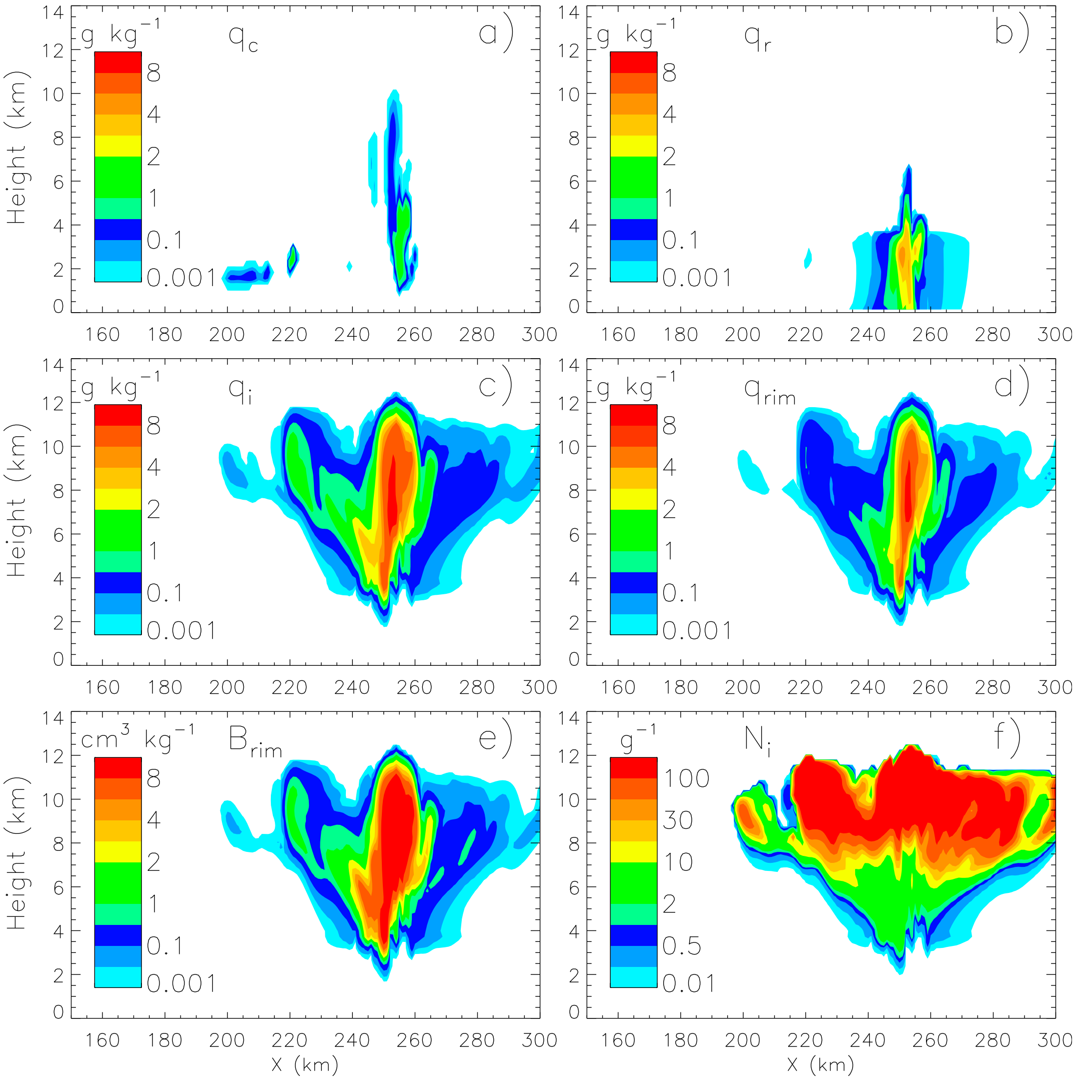

FIG. 3. Vertical cross sections for BASE at 2 h of prognostic mixing ratio quantities: (a) q_c, (b) q_r, (c) q_i, (d) q_{rim}, (e) B_{rim}, and (f) N_i.

precipitation with Z between 25 and 45 dBZ (Fig. 6a). The total storm width is about 140 km, defined by the region with $Z > 5$ dBZ at the surface. There is a large anvil region with ice mass mixing ratios up to about 1 g kg^{-1}, but areas of appreciable q_{rim} and B_{rim} are limited to the convective core region (Figs. 5c–e). The value of F_r is near 1 in the convective region (Fig. 6b) owing to the presence of substantial amounts of cloud water and rain above the freezing level (Figs. 5a,b) and hence riming and drop freezing. Below 5 km, there is a narrow core of high ρ_p (>700 kg m^{-3}) along the immediate leading edge of the storm (Fig. 6c). Aloft in the anvil and trailing stratiform region, F_r is small—generally less than 0.2 and often near 0. This indicates vapor deposition is the dominant growth mechanism there in terms of bulk mass, with growth by aggregation also contributing to an increase in D_m as particles fall from the anvil. Values of ρ_p are low (<50 kg m^{-3}) below about 6 km in this region, consistent with characteristics of large unrimed or lightly rimed aggregates. Moving from front to rear at midlevels (4–8 km) between the convective and trailing stratiform regions, there is a general decrease in D_m, F_r, ρ_p, and V_m that is consistent with size and density sorting occurring in the storm-relative front-to-rear wind flow. Overall, the growth of heavily rimed particles in the convective cores, the fallout of large rimed particles within the convective region, the detrainment of smaller ice particles to the upper anvil, and the growth of these particles primarily by vapor deposition and aggregation as they fall through the trailing stratiform region are consistent with microphysical observations and

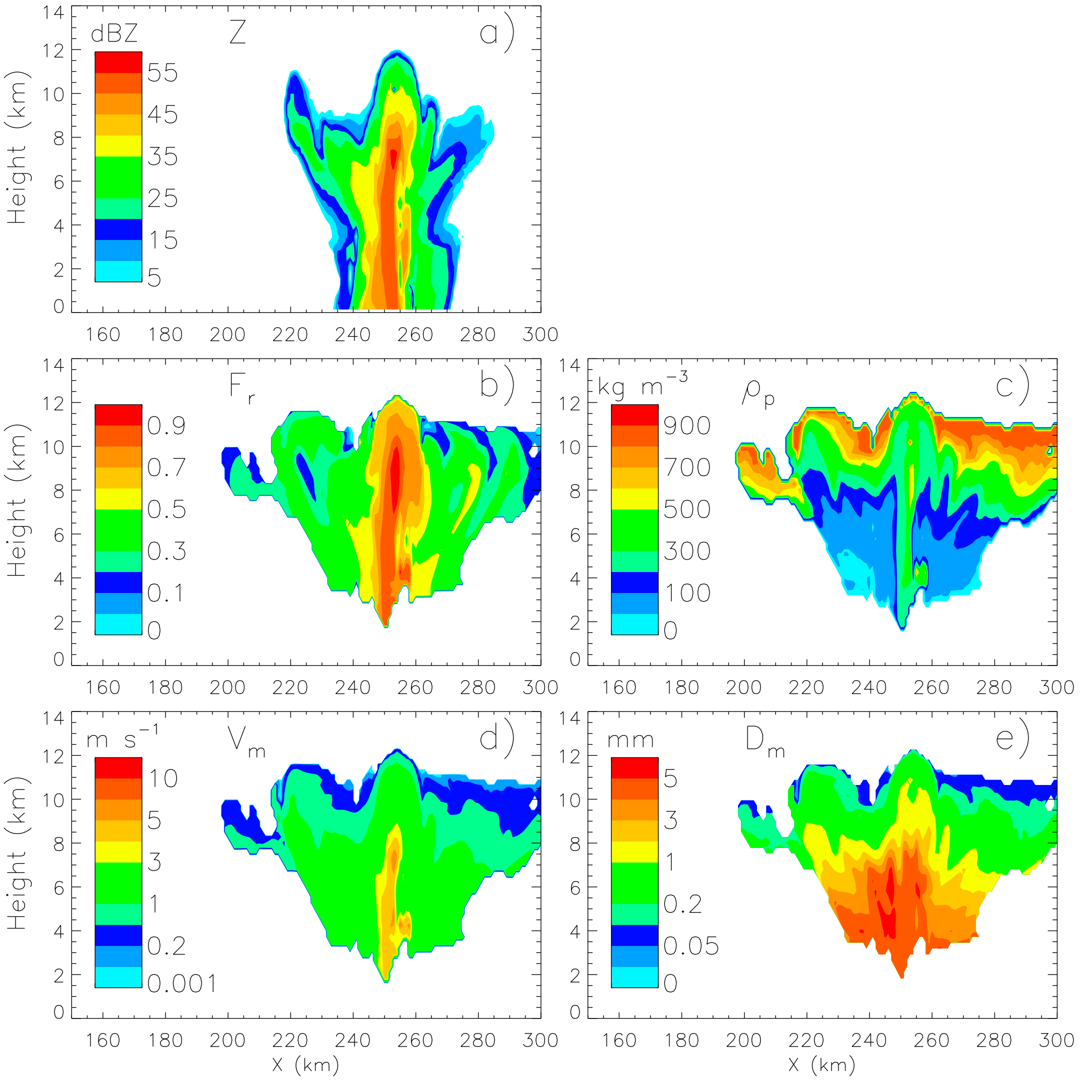

FIG. 4. Vertical cross sections for BASE at 2 h of (a) Z, (b) F_r, (c) ρ_p, (d) V_m, and (e) D_m.

retrievals of midlatitude squall lines (e.g., Rutledge and Houze 1987; Houze et al. 1989; Biggerstaff and Houze 1991, 1993; Braun and Houze 1994). In summary, by predicting important physical properties with 4 degrees of freedom, the scheme is able to simulate various types of ice-phase particles in the expected storm locations using only a single ice category.

It is also important to note that there are no obvious relationships between F_r and ρ_r and the cloud, dynamical, and thermodynamic variables such as temperature, vertical velocity, or hydrometeor mass mixing ratios prognosed in traditional microphysics schemes (Fig. 7). For example, while riming in locations with appreciable liquid water (large $q_c + q_r$), primarily in convective updrafts, is a major driver in evolving the particle properties, transport in and around updrafts leads to large F_r, ρ_r, and V_m in locations without any liquid water. Thus, even though almost all points with appreciable supercooled liquid ($q_c + q_r > 0.5\,\mathrm{g\,kg^{-1}}$) have $F_r > 0.7$, the converse is not true; that is, most points with $F_r > 0.7$ do not contain significant liquid water (Fig. 7a). These points with $F_r > 0.7$ occur near liquid water in the convective region, with rimed ice transported away from convective updrafts by air motion and sedimentation. Values of F_r from about 0.05 to 0.3 are seen in locations that are quite far (tens of kilometers) from grid points with liquid water because of horizontal transport of rimed particles in front-to-rear flow from the convective region. The transport of particles from convective updrafts several tens of kilometers is consistent with analyses from kinematic retrievals of midlatitude squall lines [e.g., see Fig. 17 in Biggerstaff and Houze (1991)]. Large scatter is also seen in the relationships

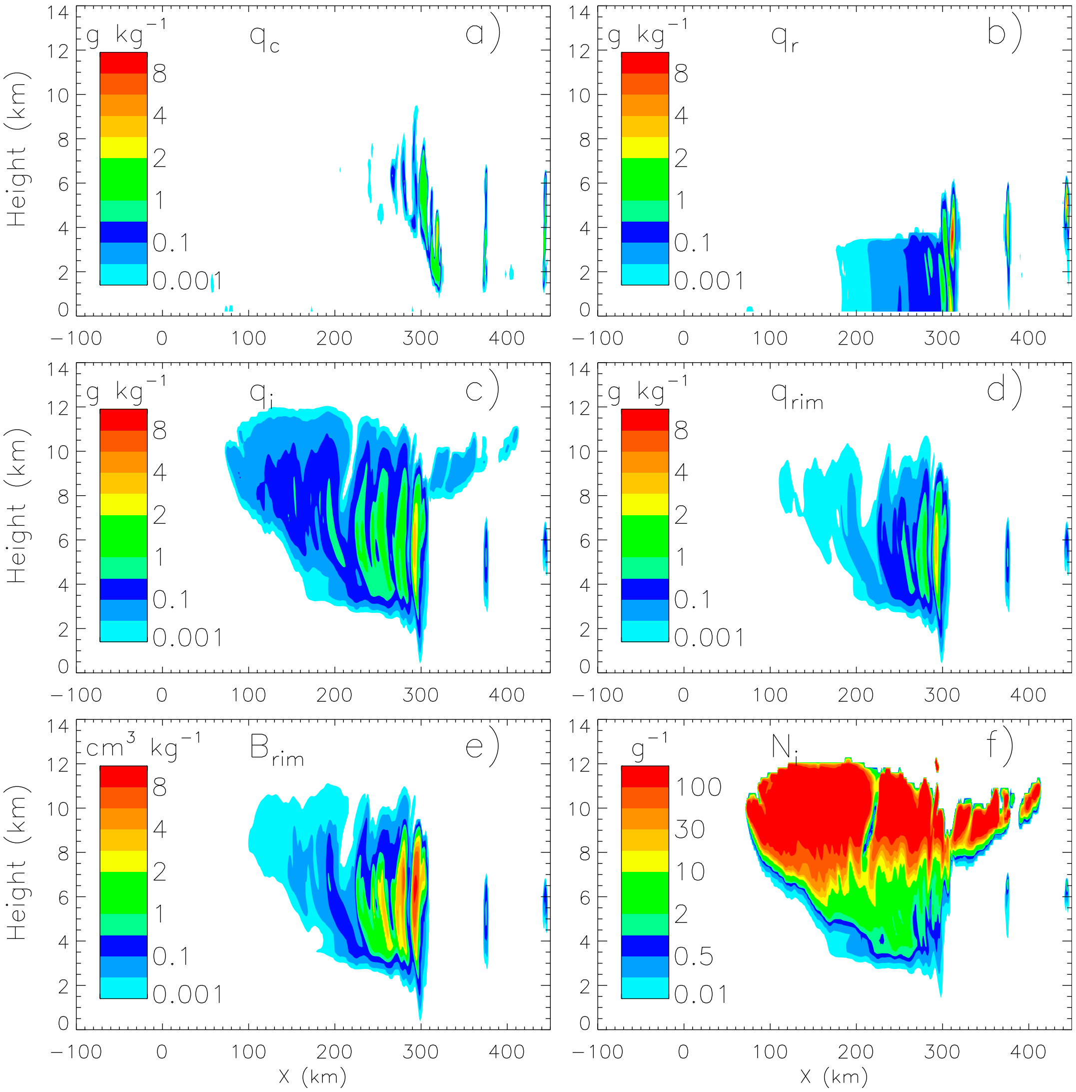

FIG. 5. As in Fig. 3, but at 6 h.

between F_r and q_i or temperature and between ρ_r and $q_c + q_r$, q_i, or temperature.

c. Sensitivity tests

To understand further the behavior of the new P3 scheme, four sensitivity tests (summarized in Table 2) were performed: 1) specification of constant $\rho_r = 400\,\mathrm{kg\,m^{-3}}$ (ρ400), 2) specification of constant $\rho_r = 900\,\mathrm{kg\,m^{-3}}$ (ρ900), 3) specification of constant $F_r = 0$ (FR0), and 4) specification of constant $F_r = 1$ and constant $\rho_r = 400\,\mathrm{kg\,m^{-3}}$ (FR1ρ400). Note that FR0 does not require specification of ρ_r since there is no rime mass in this simulation. Specified values of $\rho_r = 400$ or $900\,\mathrm{kg\,m^{-3}}$ are used here since these values are typically assumed for either the graupel or hail categories in most microphysics schemes. These sensitivity tests demonstrate the value gained by addition of q_{rim} and B_{rim} as prognostic variables, allowing for extra degrees of freedom and prediction rather than specification of ρ_r and F_r.

Figures 8–9 show vertical cross sections of ice mixing ratio and surface precipitation rate for each simulation averaged from 3.5 to 4.5 h. After 4.5 h, solutions rapidly diverge because of the initiation of convection well ahead (tens of kilometers) of the squall line, likely by gravity waves, in some of the simulations. Because of differences in storm propagation, results are shown relative to distance from the leading edge of the storm. In general, caution should be exercised when comparing results of sensitivity runs for single realizations, especially for 2D, because of rapid perturbation growth and limited inherent predictability at convective scales (e.g., Zhang et al. 2007; Wang et al. 2012). Nonetheless,

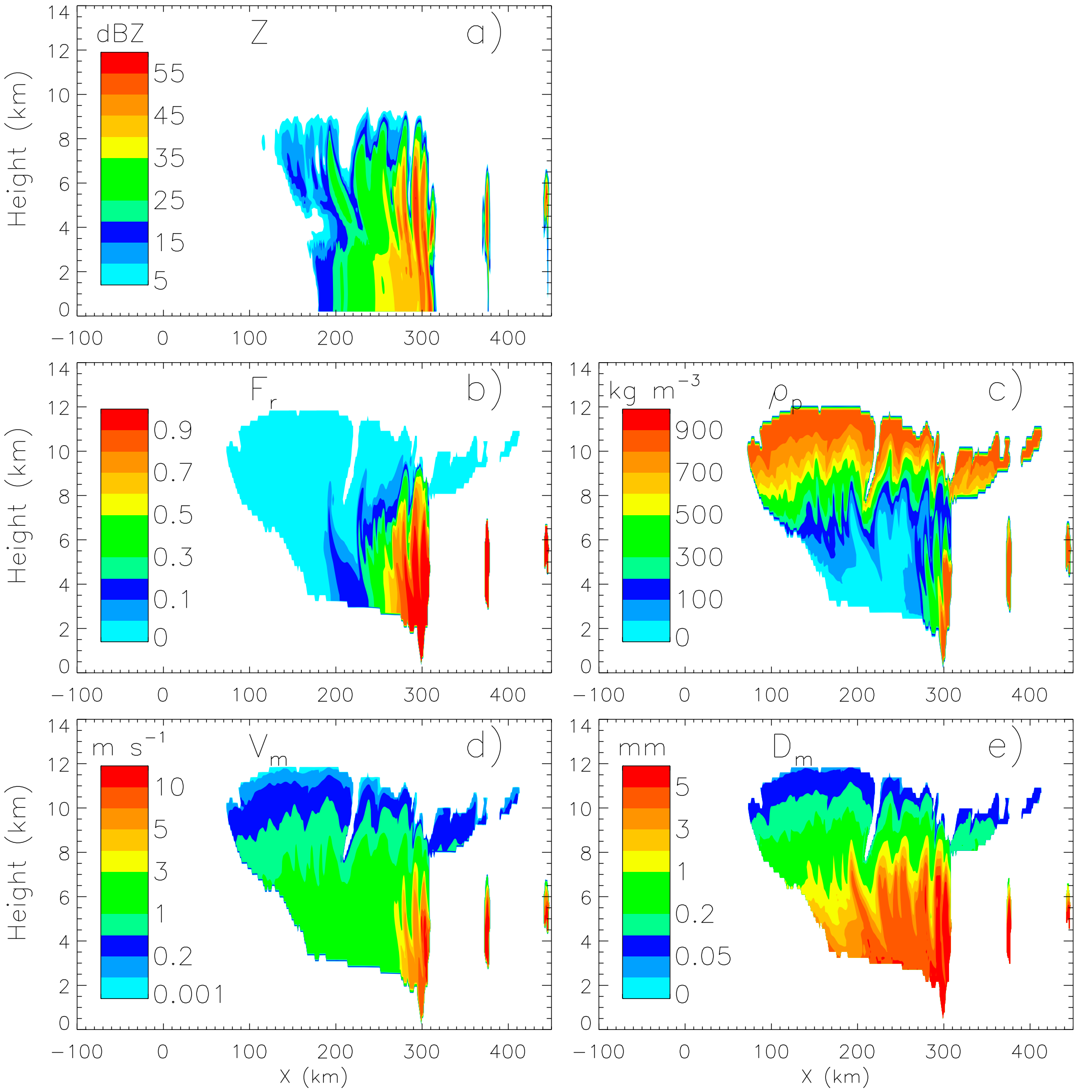

FIG. 6. As in Fig. 4, but at 6 h.

several robust differences are apparent among the simulations. Overall, there is considerable sensitivity to both F_r and ρ_r, although sensitivity to F_r is somewhat greater than to ρ_r. Ice mixing ratios in FR0 are much larger in the convective region compared to the other simulations. This results from the small V_m caused by setting $F_r = 0$, with values less than about 1.7 m s^{-1} everywhere. The value of V_m is also relatively small in the convective region in ρ400FR1 and ρ400 compared to BASE, leading to somewhat greater ice mixing ratios aloft near the leading edge, with the opposite for ρ900. Large differences are also apparent among the simulations for surface precipitation rate (Fig. 9). The ρ400 simulation exhibits a broader region of high precipitation and lacks a secondary maximum of precipitation in the trailing stratiform region, while ρ400FR1 does not have a distinct peak precipitation rate in the convective region.

4. Discussion and conclusions

A new bulk microphysics scheme has been developed that predicts various ice particle properties for a single ice-phase hydrometeor category through the use of four appropriate prognostic ice variables which are conserved during advection. Thus, various physical properties can be computed with 4 degrees of freedom. This represents a significant departure from traditional bulk schemes where ice-phase particles are partitioned into several different predefined categories with fixed properties. The proposed approach is in the spirit of recent efforts in the development of bulk schemes to predict

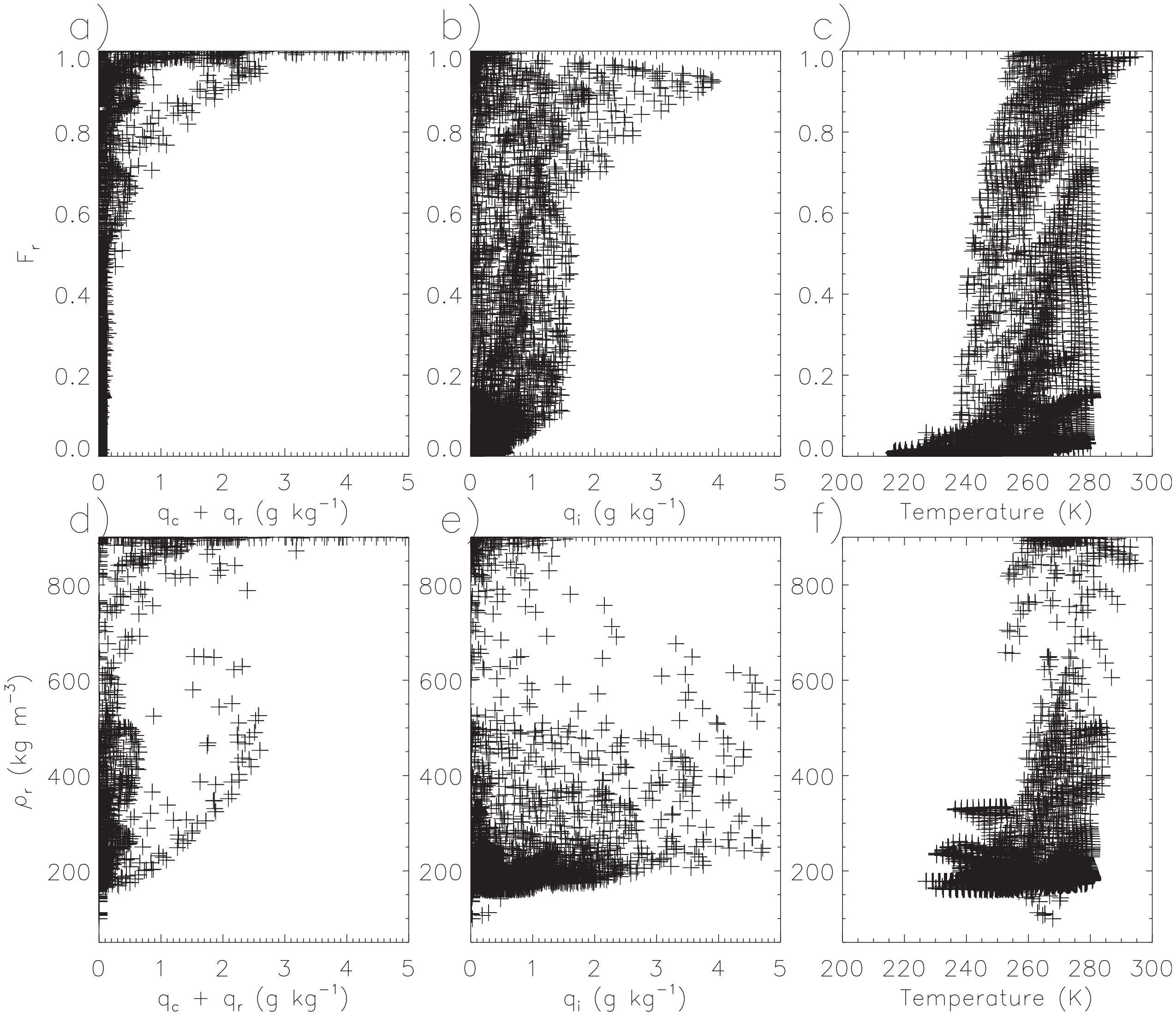

FIG. 7. Scatterplot of F_r vs (a) $q_c + q_r$, (b) q_i, and (c) temperature. (d)–(f) As in (a)–(c), respectively, but for ρ_r instead of F_r.

particle properties rather than specify them (e.g., MG08; Mansell et al. 2010; Milbrandt and Morrison 2013; Harrington et al. 2013a,b). However, it is the first such scheme to predict multiple bulk properties as ice evolves through the full range of growth processes, from initial nucleation followed by depositional growth, aggregation, and riming (including dry and wet growth) depending upon local conditions.

There are several conceptual and practical benefits of the new approach. First, it avoids the need to use poorly constrained thresholds and conversion processes between ice-phase categories, such as "autoconversion" from cloud ice to snow, that are artificial but intrinsically necessary in standard bulk schemes. It also represents a continuum of particle properties rather than discrete categories, limiting a potential source of sensitivity due to ad hoc thresholding. Since the predicted properties are real physical quantities, as opposed to unphysical parameters such as autoconversion threshold size, there is a potential for much closer coupling with observations. Finally, it is computationally efficient since the total number of prognostic ice variables is small compared to many bulk schemes. Illustration of the latter point through timing tests in the context of 3D model simulations is presented in Part II. It should be noted that this approach could also be applied to bin microphysics schemes, extending the methodology outlined by Morrison and Grabowski (2010), and would avoid the need to partition ice into predefined categories as is done in most mixed-phase bin schemes (e.g., Takahashi 1976; Reisin et al. 1996; Geresdi 1998; Khain et al. 2004; Lebo and Seinfeld 2011). Several aspects of ice

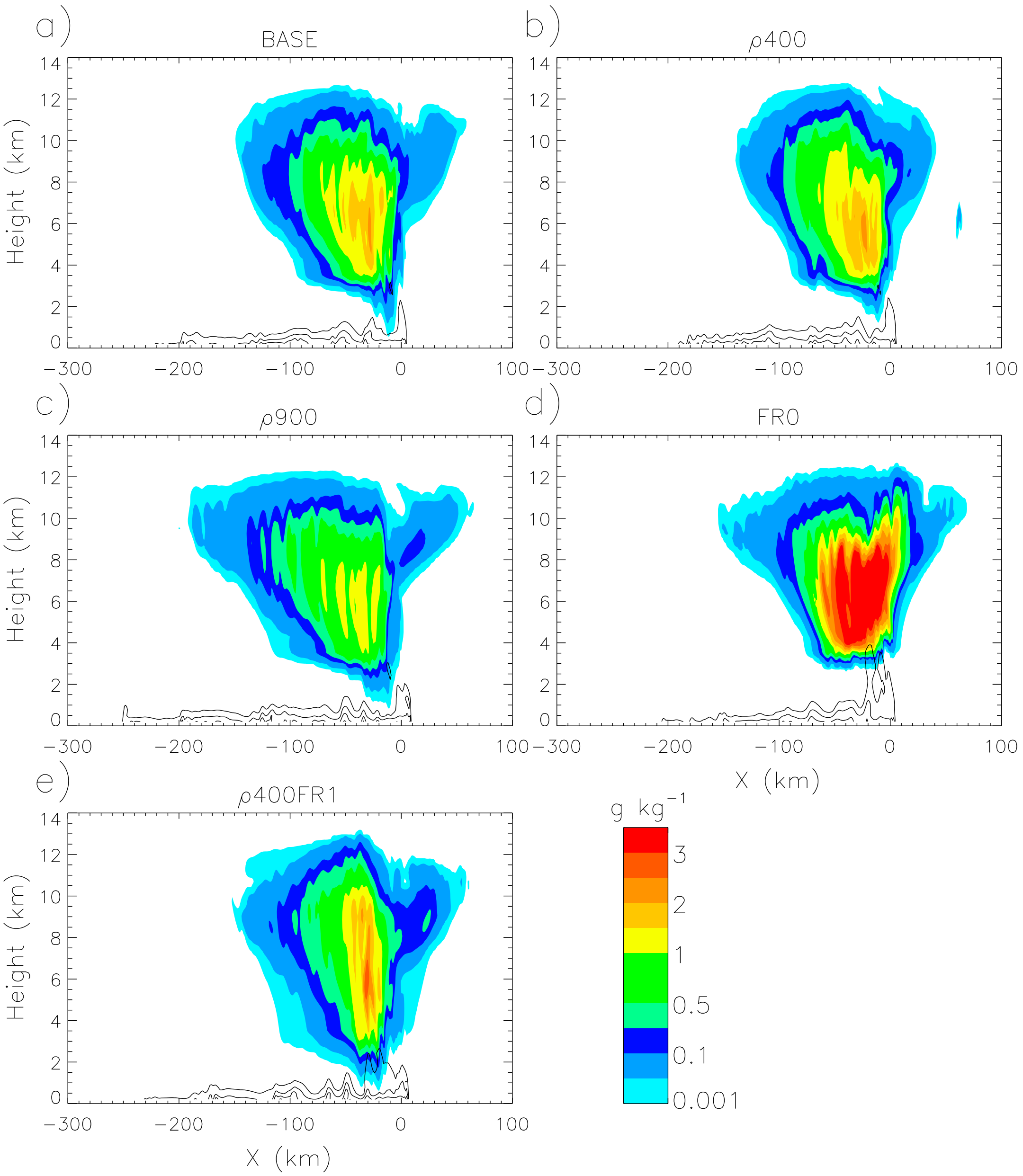

FIG. 8. Vertical cross sections of total ice water mixing ratio (color contours) averaged from 3.5 to 4.5 h as a function of distance from the leading storm edge (defined as the first grid point in the upshear direction where the surface $q_r >$ 0.001 g kg^{-1}) for the microphysics tests in Table 2. Perturbation potential temperature θ' (defined relative to the initial sounding) at 4.5 h is indicated by black contour lines, with a contour interval every 3 K for all $\theta' < -2$ K.

microphysics not addressed in this study remain uncertain, such as aggregation and riming efficiencies and parameters associated with melting and vapor diffusion. Addressing these uncertainties will require close coordination with additional observational studies, including laboratory work. While such uncertainty is unavoidable in microphysics schemes, a fundamental premise behind the P3 approach is that this uncertainty should reside in physical parameters that can be measured, at least in principle, instead of conversion parameters that are ad hoc and/or unphysical.

In the current version of P3 used in this study, the proposed approach was applied to a single ice-phase category. This does not, however, preclude the possibility of having more than one free ice-phase category, which would allow ice-phase particles with different bulk properties to be present in the same grid box and time. In such a configuration, the free ice-phase categories would

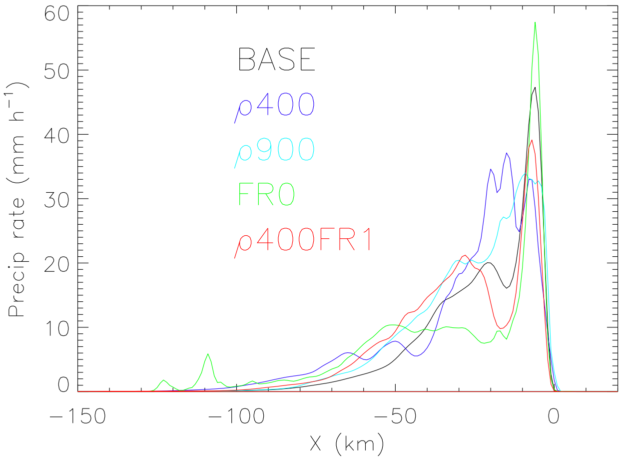

FIG. 9. Surface precipitation rate averaged from 3.5 to 4.5 h as a function of distance from the leading edge of the storm (defined as in Fig. 8) for the microphysics tests in Table 2.

not be predefined, but rather each could evolve ice to a state with any set of properties (even the same as the other categories) depending upon the growth history and conditions. This would address one of the main limitations of the current P3 scheme: its inability to represent different ice types in the same location and time for a given particle size. The development of a multiple-free-category version of the P3 scheme and comparison with the single-category version is a subject of current work and will be reported in a future publication.

Idealized 2D squall-line tests in WRF were performed to illustrate the general microphysical behavior of the new scheme. A key result is that the scheme was able to produce a wide variety of ice particle characteristics in different regions of the squall line broadly consistent with observations, despite its inclusion of only a single ice category. Sensitivity tests showed the importance of including q_{rim} and B_{rim} as prognostic variables, allowing prediction of F_r and ρ_r instead of specification of these parameters. In these tests there were notable impacts of F_r and ρ_r on the mass of ice condensate aloft and the surface precipitation rate.

The predicted properties, F_r and ρ_r in particular, exhibited no clear relationships with quantities such as cloud and rain mass mixing ratios, ice mass mixing ratio, or temperature. This is because of transport (horizontal and vertical, including sedimentation) that resulted in ice moving away from the conditions under which it experienced earlier growth. The result was rimed ice with $F_r > 0.7$ in locations without liquid water in the convective region and $F_r \sim 0.05$–0.3 for locations in the stratiform region relatively far (tens of kilometers) from liquid water. This suggests the difficulty of diagnosing particle properties from quantities as is done in some bulk schemes [e.g., Ferrier scheme in WRF; Lin et al. (2011); Lin and Colle (2011)], in contrast to adding new prognostic quantities (q_{rim}, B_{rim}) that allow for prediction of particle properties. This is likely to be especially true for high-resolution models (horizontal grid spacing of order 10 km or less) with a time scale for horizontal transport across grid cells similar to or less than the time scale for ice sedimentation. This implies, therefore, that the addition of prognostic variables is needed so that the desired particle properties can be predicted independently; diagnostic relations to reduce the number of prognostic variables do not appear to be feasible.

Finally, we note that this approach is general and other predicted properties could be added to this framework. For example, the scheme could be combined with an improved representation of vapor depositional growth to predict the crystal *a*- and *c*-axis lengths, as in Harrington et al. (2013a,b), allowing for representation of the crystal axis ratio. An improved treatment of particle evolution during melting and wet growth is possible by including prediction of the liquid water fraction on ice particles (by prognosing the liquid water mass mixing ratio on ice) (e.g., Frick et al. 2013). Prediction of the spectral width of the particle size distribution could be accomplished by the addition of a third independent moment such as reflectivity (Milbrandt and Yau 2005b). Future work will explore these ideas for continued development of the P3 scheme.

Acknowledgments. This work was partially supported by the U.S. DOE ASR DE-SC0008648, U.S. DOE ASR DE-SC0005336, sub-awarded through NASA NNX12AH90G, and the NSF Science and Technology Center for Multiscale Modeling of Atmospheric Processes (CMMAP), managed by Colorado State University under Cooperative Agreement ATM-0425247. We are grateful to T. Mansell for helpful discussions. We thank W. W. Grabowski for long-standing discussion on challenging the notion of predefined ice categories in microphysics schemes.

APPENDIX A

Overview of Liquid-Phase Component

The liquid-phase component of the scheme has prognostic variables for the mass mixing ratio of cloud droplets q_c and the mass and number mixing ratios of rain (q_r, N_r). A more detailed version of the scheme also includes prognostic equations for the cloud number mixing ratio N_c and the supersaturation and includes droplet activation on cloud condensation nuclei and cloud–aerosol interactions. This latter version of the scheme is used for the simulations described in this paper, while the former is used for the simulations in Part II. The particle size distributions (PSDs) for cloud water and rain follow the same type of gamma distribution as for ice [see (2)]. For cloud droplets, μ is based on the observations of Martin et al. (1994) as implemented in Morrison and Grabowski (2007); μ is also allowed to vary for rain. For the current implementation, μ is a function of λ following the disdrometer observations described by Cao et al. (2008):

$$\mu = -0.0201\lambda^2 + 0.902\lambda - 1.718, \qquad \text{(A1)}$$

where λ has units of per millimeter. This formula is not extrapolated to values of λ larger than the Cao et al. (2008) data range (20 mm^{-1}), giving a maximum μ of approximately 8.28. The minimum allowed μ for rain is 0.

Cloud droplet fall speed as a function of D is given by Stokes's formulation. Rain fall speed is expressed using power-law relationships as a function of $m(D)$ following Gunn and Kinzer (1949) and Beard (1976) as modified by Simmel et al. (2002). Three different power-law relationships are used for $D < 134.43\,\mu$m, $134.43 < D < 1511.64\,\mu$m, and $D > 1511.64\,\mu$m. Because different relationships are applied to different size ranges, integration of the fall speed over the PSD requires incomplete gamma functions. Since these are computationally expensive, in the code the number- and mass-weighted rain fall speeds as well as integrated ventilation parameters for vapor diffusion are precomputed and stored in a lookup table.

APPENDIX B

Microphysical Process Rates

The source/sink term S_χ for each prognostic microphysical variable in (1) is given by the following equations.

- Liquid phase:

$$\begin{aligned} S_{q_c} = {} & \text{QCNUC} + \text{QCCON} - \text{QCAUT} - \text{QCACC} \\ & - \text{QCCOL} - \text{QCHET} - \text{QCHOM} - \text{QCEVP}, \end{aligned} \qquad \text{(B1)}$$

$$\begin{aligned} S_{q_r} = {} & \text{QCAUT} + \text{QCACC} + \text{QIMLT} + \text{QCSHD} \\ & - \text{QRHET} - \text{QRHOM} - \text{QRCOL} - \text{QREVP}, \end{aligned} \qquad \text{(B2)}$$

$$\begin{aligned} S_{N_c} = {} & \text{NCNUC} - \text{NCAUT} - \text{NCACC} - \text{NCCOL} \\ & - \text{NCHET} - \text{NCHOM} - \text{NCEVP}, \quad \text{and} \end{aligned} \qquad \text{(B3)}$$

$$\begin{aligned} S_{N_r} = {} & \text{NCAUT} + \text{NRSHD} + \text{NIMLT} - \text{NRCOL} \\ & - \text{NRHET} - \text{NRHOM} - \text{NREVP}. \end{aligned} \qquad \text{(B4)}$$

- Ice phase:

$$\begin{aligned} S_{q_{\text{rim}}} = {} & \text{QCCOL} + \text{QRCOL} + \text{QCHET} \\ & + \text{QRHET} + \text{QCHOM} + \text{QRHOM} \\ & - \frac{q_{\text{rim}}(\text{QISUB} + \text{QIMLT})}{q_i}, \end{aligned} \qquad \text{(B5)}$$

$$\begin{aligned} S_{q_i} = {} & \text{QINUC} + \text{QIDEP} \\ & - \frac{(q_i - q_{\text{rim}})(\text{QISUB} + \text{QIMLT})}{q_i} + S_{q_{\text{rim}}}, \end{aligned} \qquad \text{(B6)}$$

$$\begin{aligned} S_{N_i} = {} & \text{NINUC} + \text{NCHET} + \text{NRHET} \\ & + \text{NCHOM} + \text{NRHOM} - \text{NISUB}, \quad \text{and} \end{aligned} \qquad \text{(B7)}$$

$$S_{B_r} = \frac{\text{QCHET} + \text{QCHOM} + \text{QRHET} + \text{QRHOM} + \text{QRCOL}}{\rho^*} + \frac{\text{QCCOL}}{\rho_r'} + \text{BIWET} - \frac{q_{\text{rim}}(\text{QISUB} - \text{QIMLT})}{\rho_r q_i}, \qquad \text{(B8)}$$

where ρ_r' is the density of rime collected locally at a given time (as opposed to the predicted rime density given by $\rho_r = q_{\text{rim}}/B_{\text{rim}}$); ρ_r' is calculated following Milbrandt and Morrison (2013), based on the laboratory measurements of Cober and List (1993) as a function of temperature and ice particle and drop size and fall speed.

The symbols in (B1)–(B8) represent various microphysical processes including nucleation, diffusional growth, collision–collection, freezing, and melting. The naming convention for these processes is as follows. The first letter describes whether the process involves a change in mass (Q), number (N), or volume (B) mixing ratio. For source and sink processes that do not involve multispecies interaction, the second letter indicates the species as cloud water (C), rain (R), or ice (I). For source/sink processes that involve multispecies interaction (i.e., the same process acting as a source for one species but a sink for another), the second letter (C, R, or I) indicates the species that is reduced as a result of the process. The remaining three letters indicate the type of microphysical process as defined in Table B1. Details of the microphysical process rate formulations are described in appendix C.

For simplicity, sink terms for ice (melting and sublimation) are assumed to reduce q_{rim} and q_i in proportion (i.e., the ratio q_{rim}/q_i is assumed to be unmodified by melting or sublimation). Here is it also assumed that the heterogeneous and homogeneous freezing of cloud water and rain (QCHET, QRHET, QCHOM, QRHOM) yields high-density ice and hence is included as a source for q_{rim}. This allows the model to simulate the production of high-density ice particles (i.e., embryo graupel/hail) from the freezing of liquid drops. We include freezing of cloud droplets in the production of high-density ice through QCHET and QCHOM, but this has limited impact since small ice particles are assumed to be dense ice spheres regardless of F_r or ρ_r (see section 2b).

Source terms for rime volume mixing ratio S_{B_r} are calculated by the ratio of the process rate for q_{rim} and the appropriate density. Freezing of cloud water and rain and rime generated by collection of rain by ice are assumed to produce ice with a density near solid bulk ice $\rho^* = 900\,\mathrm{kg\,m^{-3}}$. For sublimation and melting, it is assumed that bulk volume decreases in proportion with mass, i.e., density is unmodified. Wet growth [BIWET in (B8)] represents an additional sink term for B_{rim}, whereby B_{rim} decreases (i.e., particles become soaked and undergo densification) if wet growth conditions are diagnosed in subfreezing conditions (see appendix C, section g for details).

TABLE B1. Symbols used to define microphysical process rates.

AUT	Autoconversion of cloud water to rain
ACC	Accretion of cloud water by rain
NUC	Cloud droplet or ice particle nucleation
CON	Liquid condensation
EVP	Liquid evaporation
DEP	Ice deposition
SUB	Ice sublimation
COL	Collision/collection between liquid and ice
SLF	Self-collection of hydrometeors (collection within a species)
SHD	Drop shedding
HET	Heterogeneous freezing of cloud droplets and rain
HOM	Homogeneous freezing of cloud droplets and rain
MLT	Melting of ice
WET	Particle densification due to wet growth in subfreezing temperatures

APPENDIX C

The Microphysical Process Formulations

a. Droplet and crystal nucleation

In the version of the scheme with prognostic N_c, droplet activation is given by Morrison and Grabowski (2007, 2008b), assuming a constant background aerosol concentration and that the concentration of previously activated cloud condensation nuclei is equal to the local N_c. In the simulations discussed herein, the aerosol is specified as a lognormal size distribution with a total concentration of $300\,\mathrm{cm^{-3}}$ and mean size of $0.05\,\mu$m, consisting of ammonium sulfate. Condensation freezing/deposition ice nucleation follows from Cooper (1986) as a function of temperature T, as implemented in Thompson et al. (2004). Given recent evidence for limited deposition nucleation in relatively warm conditions (Ansmann et al. 2009; de Boer et al. 2011), it is limited to conditions with $T \leq 258.15\,\mathrm{K}$ and ice supersaturation $S_i \geq 5\%$. The changes in q_c from droplet activation and q_i from ice nucleation are calculated by assuming initial cloud droplet and ice crystal radii of $1\,\mu$m (with an initial ice density $\rho_i = 917\,\mathrm{kg\,m^{-3}}$).

b. Liquid condensation/evaporation and ice deposition/sublimation

The quasi-analytic formulation for supersaturation and liquid condensation/evaporation from Morrison and Grabowski (2008b) has been extended here to include the ice phase. This leads to the following expression for the time rate of change of absolute supersaturation $\delta = q - q_{\mathrm{sl}}$, where q is the water vapor mixing ratio and q_{sl} is the liquid saturation mixing ratio:

$$\frac{d\delta}{dt} = \frac{dq}{dt} - \frac{dq_{\mathrm{sl}}}{dt}\frac{dT}{dt} = A_c - \frac{\delta}{\tau}. \tag{C1}$$

Here τ is the multiphase supersaturation relaxation time scale defined by

$$\tau^{-1} = \tau_c^{-1} + \tau_r^{-1} + \left(1 + \frac{L_s}{c_p}\frac{dq_{\mathrm{sl}}}{dT}\right)\frac{\tau_i^{-1}}{\Gamma_i}, \tag{C2}$$

where τ_c, τ_r, and τ_i are the supersaturation relaxation time scales associated with cloud droplets, rain, and ice, respectively, L_s is the latent heat of sublimation, c_p is the specific heat of air at constant pressure, and Γ_i is the psychrometric correction to deposition/sublimation associated with latent heating/cooling:

$$\Gamma_i = 1 + \frac{L_s}{c_p}\frac{dq_{\mathrm{si}}}{dT}. \tag{C3}$$

Here q_{si} is the saturation vapor mixing ratio with respect to ice. In (C1), A_c is the change in δ due to vertical motion, turbulent mixing, radiation, and the Bergeron–Findeisen process:

$$A_c = \left(\frac{\partial q}{\partial t}\right)_{\mathrm{mix}} - \frac{q_{\mathrm{sl}}\rho g w}{p - e_s} - \frac{dq_{\mathrm{sl}}}{dT}\left[\left(\frac{\partial T}{\partial t}\right)_{\mathrm{rad}} + \left(\frac{\partial T}{\partial t}\right)_{\mathrm{mix}} - \frac{wg}{c_p}\right] - \frac{(q_{\mathrm{sl}} - q_{\mathrm{si}})}{\tau_i \Gamma_l}\left(1 + \frac{L_s}{c_p}\frac{dq_{\mathrm{sl}}}{dT}\right), \tag{C4}$$

where p is the air pressure, e_s is the saturation vapor pressure with respect to liquid, w is the vertical velocity, g is the acceleration of gravity, and Γ_l is as in (C3) except that L_s is replaced with L_v and q_{si} is replaced with q_{sl}. The time scales τ_c and τ_r are given by Morrison and Grabowski [2008b; see their (A5)]. For ice, τ_i follows MG08 by assuming a capacitance for that of a sphere for small spherical ice and graupel, and equal to 0.48 times that of a sphere following Field et al. (2008) for unrimed nonspherical ice. The capacitance for partially rimed crystals is linearly interpolated between values for unrimed ice and graupel based on the particle mass. Numerical integration of the appropriately weighted ice particle size distribution moment is done offline and results are stored in a lookup table.

Equation (C1) is a linear differential equation with a solution given by

$$\delta(t) = A_c\tau + (\delta_{t=0} - A_c\tau)e^{-t/\tau}, \tag{C5}$$

where $\delta_{t=0}$ is the supersaturation at the initial time.

The condensation/evaporation rate for cloud droplets is found by dividing $\delta(t)$ in (C5) by $\tau_c\Gamma_l$ to obtain the condensation/evaporation rate as a function of time and then averaging the resulting expression over the model time step (from $t = 0$ to $t = \Delta t$). This gives [(9) in Morrison and Grabowski (2008b)]

$$\mathrm{QCCON} = A_c\frac{\tau}{\tau_c\Gamma_l} + (\delta_{t=0} - A_c\tau)\frac{\tau}{\Delta t\tau_c\Gamma_l}(1 - e^{-\Delta t/\tau}). \tag{C6}$$

Similarly, the condensation/evaporation rate for rain is found by dividing $\delta(t)$ by $\tau_r\Gamma_l$ and averaging over the model time step, yielding an expression similar to (C6) except that τ_c is replaced by τ_r. For ice deposition/sublimation, the term $(q_{\mathrm{sl}} - q_{\mathrm{si}})$ is added to $\delta(t)$ in (C5) to account for the fact that it is the supersaturation with respect to ice that drives ice deposition/sublimation, and the resulting expression is divided by $\tau_i\Gamma_i$ to obtain the deposition/sublimation rate as a function of time and subsequently averaged over the model time step. This yields

$$\mathrm{QICON} = A_c\frac{\tau}{\tau_i\Gamma_i} + (\delta_{t=0} - A_c\tau)\frac{\tau}{\Delta t\tau_i\Gamma_i}(1 - e^{-\Delta t/\tau}) + \frac{(q_{\mathrm{sl}} - q_{\mathrm{si}})}{\tau_i\Gamma_i}. \tag{C7}$$

Since $\tau = \infty$ in the absence of hydrometeors, a maximum value for τ of 10^8 s is applied in the code for calculating condensation/deposition to prevent division by zero following Morrison and Grabowski (2008b).

Reduction of N_i during sublimation is scaled to the change in q_i, i.e., $(N_i/q_i) \times$ QIMLT. This is approximately equivalent to assuming a constant mean size (it is exactly equivalent if μ is constant). Reduction of N_r during evaporation is treated similarly; that is, $(\gamma_r N_r/q_r) \times$ QREVP. Here γ_r is set to 0.5, which is in the middle range of values from the parameterization of Seifert (2008). Reduction of N_c during evaporation is neglected unless all the cloud water mass within a grid point evaporates, analogous to the homogeneous mixing assumption [see discussion in Grabowski (2006)]. A more detailed approach for parameterizing the homogeneity of droplet mixing and evaporation, such as proposed by Morrison and Grabowski (2008b) and Jarecka et al. (2013), could be readily implemented into the scheme.

As discussed by Stevens et al. (1996) and Grabowski and Morrison (2008), large errors can occur in the supersaturation field when δ is derived from T and q after advection in Eulerian models because of the nonlinear dependence of q_{sl} on T. This can lead to large errors in processes that are sensitive to small changes in supersaturation—namely, droplet activation. Here we adopt the method of Grabowski and Morrison (2008) and add δ as a fully prognostic variable, including its advection. In this method, inconsistencies between T, q, and δ after advection are avoided by adjusting T and q after advection so they are consistent with the prognosed δ. This adjustment of T and q is done by condensing the exact amount of water needed to bring T and q into agreement with δ, thereby also providing a source for q_c. Because errors in δ arising from separate advection of T and q primarily impact droplet activation and hence N_c, there is less of a need to employ this method and include δ as a prognostic variable if N_c is specified. Thus, a simpler (and computationally cheaper) version of the scheme that specifies N_c and does not prognose δ has also been developed; this simpler version is used for the tests discussed in Part II.

c. *Cloud droplet autoconversion, accretion, and self-collection*

The parameterization of cloud droplet autoconversion to form rain, accretion of cloud droplets by rain, and self-collection of cloud droplets follows either Beheng (1994), Khairoutdinov and Kogan (2000), or Seifert and Beheng (2001) with a user-specified switch. Note that self-collection of droplets is not explicitly included in the Khairoutdinov and Kogan (2000) parameterization. For the tests here and in Part II, we use Khairoutdinov and Kogan (2000) for cloud water autoconversion and accretion.

d. *Raindrop self-collection and breakup*

Self-collection of rain is given by Beheng (1994). Collisional drop breakup is parameterized by reducing the collection efficiency for rain self-collection $E_{\rm cr}$ following a modified version of the Verlinde and Cotton (1993) scheme. The value of $E_{\rm cr}$ decreases with increasing mean drop size beyond a threshold size $D_{\rm rt}$:

$$\begin{aligned}&E_{\rm cr}=1, \quad D_{\rm mr}<D_{\rm rt}\\ &E_{\rm cr}=2-\exp[-2300(D_{\rm mr}-D_{\rm rt})], \quad D_{\rm mr}\geq D_{\rm rt},\end{aligned} \tag{C8}$$

where $D_{\rm mr}$ is a scaled mean raindrop size given by

$$D_{\rm mr}=4[q_r/(\pi\rho_w N_r)]^{1/3} \tag{C9}$$

and $D_{\rm rt}$ is set to 1400 μm. Note that $D_{\rm mr}$ is identical to the mass-weighted mean diameter for an exponential drop distribution. This formulation for breakup corresponds with an equilibrium (for pure breakup–coalescence) mean volume diameter (i.e., when $E_{\rm cr}=0$) of about 1100 μm, in agreement with Seifert (2008). Spontaneous raindrop breakup is treated by a simple relaxation of $D_{\rm mr}$ back to a specified mean size $D_{\rm sb}$ with a time scale $\tau_{\rm sb}$ when $D_{\rm mr}>D_{\rm sb}$. Here $D_{\rm sb}=2400\,\mu$m and $\tau_{\rm sb}=10$ s. While individual drops do not undergo spontaneous breakup until they reach rather large sizes (~5 mm) (Pruppacher and Klett 1997), it should be kept in mind that a fraction of drops will reach sizes that undergo spontaneous breakup when $D_{\rm mr}$ is smaller because the drop distribution is polydisperse, especially for wide drop size distributions (i.e., distributions that tend toward exponential shape).

e. *Collection of cloud droplets by ice*

Collection of cloud droplets by ice is parameterized using the continuous collection assumption (droplet size and fall speed are neglected in the collection kernel). The ice particle fall speed $V(D)$ and projected area $A(D)$ as described in section 2c are used to calculate the collection kernel. Because of the complicated dependence of $V(D)$ and $A(D)$ on D, the appropriately weighted moment of the ice particle size distribution corresponding to collection of liquid is calculated offline and stored in lookup table as a function of q_i, N_i, F_r, and ρ_r. The collection efficiency is specified to be unity. At temperatures above freezing the collected mass of cloud droplets is shed assuming a shed drop size of 1 mm following Rasmussen et al. (1984). At temperatures below freezing, the collected droplets are assumed to freeze instantaneously except in wet growth conditions as described in section g of this appendix.

f. *Collisions between rain and ice*

Changes in number and mass mixing ratio resulting from collisions between rain and ice use a collection kernel derived from $A(D)$ and $V(D)$ for ice and rain numerically integrated over the ice and rain size distributions. Collisions between rain and ice are calculated for all ice particle and rain drop sizes across the respective distributions. Because of the numerical integration, the integrated collision kernels are calculated offline and stored in a lookup table as a function of q_i, N_i, F_r, ρ_r and a scaled mean raindrop size proportional to $(q_r/N_r)^{1/3}$. The collection efficiency is assumed to be unity. At temperatures above freezing, the mass of rain that collides with ice is shed assuming a shed drop size of 1 mm. At temperatures below freezing, the rain mass that collides with ice is assumed to freeze instantaneously except in wet growth conditions as described in section g of this appendix.

g. *Wet growth of ice*

In conditions with relatively warm temperatures and large riming rates, ice particle surface temperatures can reach 273.15 K. In this case not all of the collected liquid water is frozen and instead some fraction is shed. We calculate the wet growth rate following Musil (1970), numerically integrated over the ice particle size distribution. Values are precomputed and stored in a lookup table. When the dry growth rate is smaller than the wet growth rate all collected water is assumed to freeze instantaneously. When the dry growth rate exceeds the wet growth rate the difference between the rates is shed as 1-mm-sized raindrops. If wet growth conditions are diagnosed, then particles also become soaked and undergo densification with $B_r=q_{\rm rim}/\rho^*$, where $\rho^*=900$ kg m^{-3}. This densification is assumed to occur within one time step. We also note the role of soaking and particle densification during melting in conditions above freezing but leave a detailed treatment of particle evolution during melting for future work.

h. *Freezing of cloud droplets and rain*

Heterogeneous freezing of cloud droplets and rain follows from the volume-dependent formulation from Bigg (1953) but with parameters following Barklie and Gokhale (1959) [see also Pruppacher and Klett (1997, p. 350)]. Homogeneous freezing of cloud droplets and rain occurs instantaneously at 233.15 K.

i. *Melting*

Melting is treated using the simplified diffusion approximation including ventilation and environmental relative humidity effects similar to Lin et al. (1983) and others. The appropriate moment of the ice particle size distribution is numerically integrated offline and stored in a lookup table. Reduction of N_i during melting is scaled to the change in q_i, i.e., $(N_i/q_i) \times$ QIMLT. Each melted ice particle is assumed to produce a single raindrop.

j. *Sedimentation*

The prognostic variables sediment at appropriate moment-weighted terminal fall speeds. The total mass, rime mass, and rime volume mixing ratios use the mass (total)-weighted fall speed

$$V_m = \frac{\int_0^\infty V(D)m(D)N'(D)\,dD}{\int_0^\infty m(D)N'(D)\,dD}, \qquad \text{(C10)}$$

while the number mixing ratio uses the number-weighted fall speed

$$V_N = \frac{\int_0^\infty V(D)N'(D)\,dD}{\int_0^\infty N'(D)\,dD}. \qquad \text{(C11)}$$

REFERENCES

Adams-Selin, R. D., S. C. van den Heever, and R. H. Johnson, 2013: Impacts of graupel parameterization schemes on idealized bow echo simulations. *Mon. Wea. Rev.,* **141,** 3735–3756, doi:10.1175/MWR-D-12-00343.1.

Ansmann, A., and Coauthors, 2009: Evolution of the ice phase in tropical altocumulus: SAMUM lidar observations over Cape Verde. *J. Geophys. Res.,* **114,** D17208, doi:10.1029/2008JD011659.

Barklie, R. H. D., and N. R. Gokhale, 1959: The freezing of supercooled water drops. Alberta hail, 1958, and related studies, McGill University Stormy Weather Group Sci. Rep. MW-30, Part III, 43–64.

Beard, K. V., 1976: Terminal velocity and shape of cloud and precipitation drops aloft. *J. Atmos. Sci.,* **33,** 851–864, doi:10.1175/1520-0469(1976)033<0851:TVASOC>2.0.CO;2.

Beheng, K. D., 1994: A parameterization of warm cloud microphysical conversion processes. *Atmos. Res.,* **33,** 193–206, doi:10.1016/0169-8095(94)90020-5.

Berry, E., and R. Reinhardt, 1974: An analysis of cloud drop growth by collection: Part II. Single initial distributions. *J. Atmos. Sci.,* **31,** 1825–1831, doi:10.1175/1520-0469(1974)031<1825:AAOCDG>2.0.CO;2.

Bigg, E. K., 1953: The supercooling of water. *Proc. Phys. Soc.,* **66B,** 688–694, doi:10.1088/0370-1301/66/8/309.

Biggerstaff, M. I., and R. A. Houze, 1991: Kinematic and precipitation structure of the 10–11 June 1985 squall line. *Mon. Wea. Rev.,* **119,** 3034–3065, doi:10.1175/1520-0493(1991)119<3034:KAPSOT>2.0.CO;2.

——, and ——, 1993: Kinematics and microphysics of the transition zone of the 10–11 June 1985 squall line. *J. Atmos. Sci.,* **50,** 3091–3110, doi:10.1175/1520-0469(1993)050<3091:KAMOTT>2.0.CO;2.

Braun, S. A., and R. A. Houze, 1994: The transition zone and secondary maximum of radar reflectivity behind a midlatitude squall line: Results retrieved from Doppler radar data. *J. Atmos. Sci.,* **51,** 2733–2755, doi:10.1175/1520-0469(1994)051<2733:TTZASM>2.0.CO;2.

Brown, P. R. A., and P. N. Francis, 1995: Improved measurements of the ice water content in cirrus using a total water probe. *J. Atmos. Oceanic Technol.,* **12,** 410–414, doi:10.1175/1520-0426(1995)012<0410:IMOTIW>2.0.CO;2.

Bryan, G., and H. Morrison, 2012: Sensitivity of a simulated squall line to horizontal resolution and parameterization of microphysics. *Mon. Wea. Rev.,* **140,** 202–225, doi:10.1175/MWR-D-11-00046.1.

Cao, Q., G. Zhang, E. Brandes, T. Schuur, A. Ryzhkov, and K. Ikeda, 2008: Analysis of video disdrometer and polarimetric radar data to characterize rain microphysics in Oklahoma. *J. Appl. Meteor. Climatol.,* **47,** 2238–2255, doi:10.1175/2008JAMC1732.1.

Cober, S. G., and R. List, 1993: Measurements of the heat and mass transfer parameters characterizing conical graupel growth. *J. Atmos. Sci.,* **50,** 1591–1609, doi:10.1175/1520-0469(1993)050<1591:MOTHAM>2.0.CO;2.

Cohard, J.-M., and J.-P. Pinty, 2000: A comprehensive two-moment warm microphysical bulk scheme. I: Description and tests. *Quart. J. Roy. Meteor. Soc.,* **126,** 1815–1842, doi:10.1256/smsqj.56613.

Cohen, C., and E. W. McCaul Jr., 2006: The sensitivity of simulated convective storms to variations in prescribed single-moment microphysics parameters that describe particle distributions, sizes, and numbers. *Mon. Wea. Rev.,* **134,** 2547–2565, doi:10.1175/MWR3195.1.

Colle, B. A., M. F. Garvert, J. B. Wolfe, C. F. Mass, and C. P. Woods, 2005: The 13–14 December 2001 IMPROVE-2 event. Part III: Simulated microphysical budgets and sensitivity studies. *J. Atmos. Sci.,* **62,** 3535–3558, doi:10.1175/JAS3552.1.

Connolly, P. J., T. W. Choularton, M. W. Gallagher, K. N. Bower, M. J. Flynn, and J. A. Whiteway, 2006: Cloud-resolving simulations of intense tropical Hector thunderstorms: Implications for aerosol–cloud interactions. *Quart. J. Roy. Meteor. Soc.,* **132,** 3079–3106, doi:10.1256/qj.05.86.

Cooper, W. A., 1986: Ice initiation in natural clouds. *Precipitation Enhancement—A Scientific Challenge, Meteor. Monogr.,* No. 43, Amer. Meteor. Soc., 29–32.

Dawson, D. T., II, M. Xue, J. A. Milbrandt, and M. K. Yau, 2010: Comparison of evaporation and cold pool development between single-moment and multi-moment bulk microhysics schemes in idealized simulations of tornadic thunderstorms. *Mon. Wea. Rev.,* **138,** 1152–1171, doi:10.1175/2009MWR2956.1.

de Boer, G., H. Morrison, M. D. Shupe, and R. Hildner, 2011: Evidence of liquid dependent ice nucleation in high-latitude stratiform clouds from surface remote sensors. *Geophys. Res. Lett.,* **38,** L01803, doi:10.1029/2010GL046016.

Ferrier, B. S., 1994: A double-moment multiple-phase four-class bulk ice scheme. Part I: Description. *J. Atmos. Sci.,* **51,** 249–280, doi:10.1175/1520-0469(1994)051<0249:ADMMPF>2.0.CO;2.

Field, P. R., A. J. Heymsfield, A. Bansemer, and C. H. Twohy, 2008: Determination of the combined ventilation factor and capacitance for ice crystal aggregates in airborne observations in a tropical anvil cloud. *J. Atmos. Sci.,* **65,** 376–391, doi:10.1175/2007JAS2391.1.

Frick, C., A. Seifert, and H. Wernli, 2013: A bulk parameterization of melting snowflakes with explicit water fraction for the COSMO model. *Geosci. Model Dev.,* **6,** 1925–1939, doi:10.5194/gmd-6-1925-2013.

Geresdi, I., 1998: Idealized simulation of the Colorado hailstorm case: Comparison of bulk and detailed microphysics. *Atmos. Res.,* **45,** 237–252, doi:10.1016/S0169-8095(97)00079-3.

Gilmore, M. S., J. M. Straka, and E. N. Rasmussen, 2004: Precipitation uncertainty due to variations in precipitation particle parameters within a simple microphysics scheme. *Mon. Wea. Rev.,* **132,** 2610–2627, doi:10.1175/MWR2810.1.

Grabowski, W. W., 2006: Indirect impact of atmospheric aerosols in idealized simulations of convective-radiative equilibrium. *J. Climate,* **19,** 4664–4682, doi:10.1175/JCLI3857.1.

——, and H. Morrison, 2008: Toward the mitigation of spurious cloud-edge supersaturation in cloud models. *Mon. Wea. Rev.,* **136,** 1224–1234, doi:10.1175/2007MWR2283.1.

Gunn, R., and G. D. Kinzer, 1949: The terminal velocity of fall for water droplets in stagnant air. *J. Meteor.,* **6,** 243–244, doi:10.1175/1520-0469(1949)006<0243:TTVOFF>2.0.CO;2.

Hallett, J., and S. C. Mossop, 1974: Production of secondary ice particles during the riming process. *Nature,* **249,** 26–28, doi:10.1038/249026a0.

Harrington, J. Y., K. Sulia, and H. Morrison, 2013a: A method for adaptive habit prediction in bulk microphysical models. Part I: Theoretical development. *J. Atmos. Sci.,* **70,** 349–364, doi:10.1175/JAS-D-12-040.1.

——, ——, and ——, 2013b: A method for adaptive habit prediction in bulk microphysical models. Part II: Parcel model corroboration. *J. Atmos. Sci.,* **70,** 365–376, doi:10.1175/JAS-D-12-0152.1.

Hashino, T., and G. J. Tripoli, 2007: The Spectral Ice Habit Prediction System (SHIPS). Part I: Model description and simulation of the vapor deposition process. *J. Atmos. Sci.,* **64,** 2210–2237, doi:10.1175/JAS3963.1.

Heymsfield, A. J., 1982: A comparative study of the rates of development of potential graupel and hail embryos in High Plains storms. *J. Atmos. Sci.,* **39,** 2867–2897, doi:10.1175/1520-0469(1982)039<2867:ACSOTR>2.0.CO;2.

——, 2003: Properties of tropical and midlatitude ice cloud particle ensembles. Part II: Applications for mesoscale and climate models. *J. Atmos. Sci.,* **60,** 2592–2611, doi:10.1175/1520-0469(2003)060<2592:POTAMI>2.0.CO;2.

——, A. Bansemer, and C. H. Twohy, 2007: Refinements to ice particle mass dimensional and terminal velocity relationships for ice clouds. Part I: Temperature dependence. *J. Atmos. Sci.,* **64,** 1047–1067, doi:10.1175/JAS3890.1.

Houze, R. A., M. I. Biggerstaff, S. A. Rutledge, and B. F. Smull, 1989: Interpretation of Doppler weather radar displays of midlatitude mesoscale convective systems. *Bull. Amer. Meteor. Soc.,* **70,** 608–619, doi:10.1175/1520-0477(1989)070<0608:IODWRD>2.0.CO;2.

Jarecka, D., W. W. Grabowski, H. Morrison, and H. Pawlowska, 2013: Homogeneity of the subgrid-scale turbulent mixing in large-eddy simulation of shallow convection. *J. Atmos. Sci.,* **70,** 2751–2767, doi:10.1175/JAS-D-13-042.1.

Kessler, E., 1969: *On the Distribution and Continuity of Water Substance in Atmosphere Circulations. Meteor. Monogr.,* No. 32, Amer. Meteor. Soc., 84 pp.

Khain, A., A. Pokrovsky, M. Pinsky, A. Seifert, and V. Phillips, 2004: Simulation of effects of atmospheric aerosols on deep turbulent convective clouds using a spectral microphysics mixed-phase cumulus cloud model. Part I: Model description and possible application. *J. Atmos. Sci.,* **61,** 2963–2982, doi:10.1175/JAS-3350.1.

Khairoutdinov, M. F., and Y. Kogan, 2000: A new cloud physics parameterization in a large-eddy simulation model of marine stratocumulus. *Mon. Wea. Rev.,* **128,** 229–243, doi:10.1175/1520-0493(2000)128<0229:ANCPPI>2.0.CO;2.

Khvorostyanov, V. I., and J. A. Curry, 2002: Terminal velocities of droplets and crystals: Power laws with continuous parameters over the size spectrum. *J. Atmos. Sci.,* **59,** 1872–1884, doi:10.1175/1520-0469(2002)059<1872:TVODAC>2.0.CO;2.

Koenig, L. R., and F. W. Murray, 1976: Ice-bearing cumulus cloud evolution: Numerical simulation and general comparison against observations. *J. Appl. Meteor.,* **15,** 747–762, doi:10.1175/1520-0450(1976)015<0747:IBCCEN>2.0.CO;2.

Kogan, Y. L., and A. Belochitski, 2012: Parameterization of cloud microphysics based on full integral moments. *J. Atmos. Sci.,* **69,** 2229–2242, doi:10.1175/JAS-D-11-0268.1.

Lang, S., W.-K. Tao, and X. Zeng, 2011: Reducing the biases in simulated radar reflectivities from a bulk microphysics scheme: Tropical convective systems. *J. Atmos. Sci.,* **68,** 2306–2320, doi:10.1175/JAS-D-10-05000.1.

Lebo, Z., and J. H. Seinfeld, 2011: Theoretical basis for convective invigoration due to increased aerosol concentration. *Atmos. Chem. Phys.,* **11,** 5407–5429, doi:10.5194/acp-11-5407-2011.

Lim, K.-S. S., and S.-Y. Hong, 2010: Development of an effective double-moment cloud microphysics scheme with prognostic cloud condensation nuclei (CCN) for weather and climate models. *Mon. Wea. Rev.,* **138,** 1587–1612, doi:10.1175/2009MWR2968.1.

Lin, Y., and B. A. Colle, 2011: A new bulk microphysical scheme that includes riming intensity and temperature-dependent ice characteristics. *Mon. Wea. Rev.,* **139,** 1013–1035, doi:10.1175/2010MWR3293.1.

——, L. J. Donner, and B. A. Colle, 2011: Parameterization of riming intensity and its impact on ice fall speed using ARM data. *Mon. Wea. Rev.,* **139,** 1036–1047, doi:10.1175/2010MWR3299.1.

Lin, Y.-L., R. D. Farley, and H. D. Orville, 1983: Bulk parameterization of the snow field in a cloud model. *J. Climate Appl. Meteor.,* **22,** 1065–1092, doi:10.1175/1520-0450(1983)022<1065:BPOTSF>2.0.CO;2.

Locatelli, J. D., and P. V. Hobbs, 1974: Fall speeds and masses of solid precipitation particles. *J. Geophys. Res.,* **79,** 2185–2197, doi:10.1029/JC079i015p02185.

Mansell, E. R., C. L. Ziegler, and E. C. Bruning, 2010: Simulated electrification of a small thunderstorm with two-moment bulk microphysics. *J. Atmos. Sci.,* **67,** 171–194, doi:10.1175/2009JAS2965.1.

Martin, G. M., D. W. Johnson, and A. Spice, 1994: The measurement and parameterization of effective radius of droplets in warm stratocumulus clouds. *J. Atmos. Sci.,* **51,** 1823–1842, doi:10.1175/1520-0469(1994)051<1823:TMAPOE>2.0.CO;2.

Matson, R. J., and A. W. Huggins, 1980: The direct measurement of the sizes, shapes and kinematics of falling hailstones. *J. Atmos. Sci.,* **37,** 1107–1125, doi:10.1175/1520-0469(1980)037<1107:TDMOTS>2.0.CO;2.

McCumber, M., W.-K. Tao, J. Simpson, R. Penc, and S.-T. Soong, 1991: Comparison of ice-phase microphysical parameterization schemes using numerical simulations of tropical convection. *J. Appl. Meteor.,* **30,** 985–1004, doi:10.1175/1520-0450-30.7.985.

McFarquhar, G. M., H. Zhang, G. Heymsfield, R. Hood, J. Dudhia, J. B. Halverson, and F. Marks Jr., 2006: Factors affecting the evolution of Hurricane Erin (2001) and the distributions of hydrometeors: Role of microphysical processes. *J. Atmos. Sci.,* **63,** 127–150, doi:10.1175/JAS3590.1.

Meyers, M. P., R. L. Walko, J. Y. Harrington, and W. R. Cotton, 1997: New RAMS cloud microphysics. Part II: The two-moment scheme. *Atmos. Res.,* **45,** 3–39, doi:10.1016/S0169-8095(97)00018-5.

Milbrandt, J. A., and M. K. Yau, 2005a: A multimoment bulk microphysics parameterization. Part I: Analysis of the role of the spectral shape parameter. *J. Atmos. Sci.,* **62,** 3051–3064, doi:10.1175/JAS3534.1.

——, and ——, 2005b: A multimoment bulk microphysics parameterization. Part II: A proposed three-moment closure and scheme description. *J. Atmos. Sci.,* **62,** 3065–3081, doi:10.1175/JAS3535.1.

——, and R. McTaggart-Cowan, 2010: Sedimentation-induced errors in bulk microphysics schemes. *J. Atmos. Sci.,* **67,** 3931–3948, doi:10.1175/2010JAS3541.1.

——, and H. Morrison, 2013: Predicting graupel density in a bulk microphysics scheme. *J. Atmos. Sci.,* **70,** 410–429, doi:10.1175/JAS-D-12-0204.1.

Mitchell, D. L., 1996: Use of mass- and area-dimensional power laws for determining precipitation particle terminal velocities. *J. Atmos. Sci.,* **53,** 1710–1723, doi:10.1175/1520-0469(1996)053<1710:UOMAAD>2.0.CO;2.

——, and A. J. Heymsfield, 2005: The treatment of ice particle terminal velocities, highlighting aggregates. *J. Atmos. Sci.,* **62,** 1637–1644, doi:10.1175/JAS3413.1.

——, and E. Erfani, cited 2014: Developing and bounding ice particle mass- and area-dimension expressions for use in climate models and remote sensing. [Available online at https://ams.confex.com/ams/14CLOUD14ATRAD/webprogram/Paper250163.html.]

——, R. Zhang, and R. L. Pitter, 1990: Mass-dimensional relationships for ice particles and the influence of riming on snowfall rates. *J. Appl. Meteor.,* **29,** 153–163, doi:10.1175/1520-0450(1990)029<0153:MDRFIP>2.0.CO;2.

Morrison, H., 2012: On the numerical treatment of hydrometeor sedimentation in bulk and hybrid bulk–bin schemes. *Mon. Wea. Rev.,* **140,** 1572–1588, doi:10.1175/MWR-D-11-00140.1.

——, and W. W. Grabowski, 2007: Comparison of bulk and bin warm rain microphysics models using a kinematic framework. *J. Atmos. Sci.,* **64,** 2839–2861, doi:10.1175/JAS3980.

——, and ——, 2008a: A novel approach for representing ice microphysics in models: Description and tests using a kinematic framework. *J. Atmos. Sci.,* **65,** 1528–1548, doi:10.1175/2007JAS2491.1.

——, and ——, 2008b: Modeling supersaturation and subgrid-scale mixing with two-moment warm bulk microphysics. *J. Atmos. Sci.,* **65,** 792–812, doi:10.1175/2007JAS2374.1.

——, and ——, 2010: An improved representation of rimed snow and conversion to graupel in a mutlicomponent bin microphysics scheme. *J. Atmos. Sci.,* **67,** 1337–1360, doi:10.1175/2010JAS3250.1.

——, and J. A. Milbrandt, 2011: Comparison of two-moment bulk microphysics schemes in idealized supercell thunderstorm simulations. *Mon. Wea. Rev.,* **139,** 1103–1130, doi:10.1175/2010MWR3433.1.

——, J. A. Curry, and V. I. Khvorostyanov, 2005: A new double-moment microphysics parameterization for application in cloud and climate models. Part I: Description. *J. Atmos. Sci.,* **62,** 1665–1677, doi:10.1175/JAS3446.1.

——, G. Thompson, and V. Tatarskii, 2009: Impact of cloud microphysics on the development of trailing stratiform precipitation in a simulated squall line: Comparison of one- and two-moment schemes. *Mon. Wea. Rev.,* **137,** 991–1007, doi:10.1175/2008MWR2556.1.

——, J. A. Milbrandt, G. H. Bryan, K. Ikeda, S. A. Tessendorf, and G. Thompson, 2015: Parameterization of microphysics based on the prediction of bulk ice particle properties. Part II: Case study comparisons with observations and other schemes. *J. Atmos. Sci.,* **72,** 312–339, doi:10.1175/JAS-D-14-0066.1.

Musil, D. J., 1970: Computer modeling of hailstone growth in feeder clouds. *J. Atmos. Sci.,* **27,** 474–482, doi:10.1175/1520-0469(1970)027<0474:CMOHGI>2.0.CO;2.

Philips, V. T. J., L. J. Donner, and S. T. Garner, 2007: Nucleation processes in deep convection simulated by a cloud-resolving model with double-moment bulk microphysics. *J. Atmos. Sci.,* **64,** 738–761, doi:10.1175/JAS3869.1.

Pruppacher, H. R., and J. D. Klett, 1997: *Microphysics of Clouds and Precipitation.* Kluwer Academic Publishers, 954 pp.

Rasmussen, R. M., V. Levizzani, and H. R. Pruppacher, 1984: A wind tunnel and theoretical study on the melting behavior of atmospheric ice particles: III. Experiment and theory for spherical ice particles of radius > 500 μm. *J. Atmos. Sci.,* **41,** 381–388, doi:10.1175/1520-0469(1984)041<0381:AWTATS>2.0.CO;2.

Reisin, T., Z. Levin, and S. Tzivion, 1996: Rain production in convective clouds as simulated in an axisymmetric model with detailed microphysics. Part I: Description of the model. *J. Atmos. Sci.,* **53,** 497–519, doi:10.1175/1520-0469(1996)053<0497:RPICCA>2.0.CO;2.

Reisner, J., R. M. Rasmussen, and R. T. Bruintjes, 1998: Explicit forecasting of supercooled liquid water in winter storms using the MM5 mesoscale model. *Quart. J. Roy. Meteor. Soc.,* **124,** 1071–1107, doi:10.1002/qj.49712454804.

Rogers, D. C., 1974: The aggregation of natural ice crystals. Rep. AR110, 91 pp. [Available from University of Wyoming, Atmospheric Science, Dept. 3038, 1000 E. University Ave., Laramie, WY 82072.]

Rutledge, S. A., and P. V. Hobbs, 1983: The mesoscale and microscale structure and organization of clouds and precipitation in midlatitude cyclones. VII: A model for the "seeder-feeder" process in warm-frontal rainbands. *J. Atmos. Sci.,* **40,** 1185–1206, doi:10.1175/1520-0469(1983)040<1185:TMAMSA>2.0.CO;2.

——, and ——, 1984: The mesoscale and microscale structure and organization of clouds and precipitation in midlatitude cyclones. XII: A diagnostic modeling study of precipitation development in narrow cold-frontal rainbands. *J. Atmos. Sci.,* **41,** 2949–2972, doi:10.1175/1520-0469(1984)041<2949:TMAMSA>2.0.CO;2.

——, and R. A. Houze, 1987: A diagnostic modelling study of the trailing stratiform region of a midlatitude squall line. *J. Atmos. Sci.,* **44,** 2640–2656, doi:10.1175/1520-0469(1987)044<2640:ADMSOT>2.0.CO;2.

Schmitt, C. G., and A. J. Heymsfield, 2010: Dimensional characteristics of ice crystal aggregates from fractal geometry. *J. Atmos. Sci.,* **67,** 1605–1616, doi:10.1175/2009JAS3187.1.

Seifert, A., 2008: On the parameterization of evaporation of raindrops as simulated by a one-dimensional rainshaft model. *J. Atmos. Sci.,* **65,** 3608–3619, doi:10.1175/2008JAS2586.1.

——, and K. D. Beheng, 2001: A double-moment parameterization for simulating autoconversion, accretion and selfcollection. *Atmos. Res.,* **59–60,** 265–281, doi:10.1016/S0169-8095(01)00126-0.

Simmel, M., T. Trautmann, and G. Tetzlaff, 2002: Numerical solution of the stochastic collection equation comparison of the linear discrete method with other methods. *Atmos. Res.,* **61,** 135–148, doi:10.1016/S0169-8095(01)00131-4.

Skamarock, W. C., and Coauthors, 2008: A description of the Advanced Research WRF version 3. NCAR Tech. Note TN-475+STR, 113 pp. [Available online at http://www.mmm.ucar.edu/wrf/users/docs/arw_v3_bw.pdf.]

Smith, P. L., 1984: Equivalent radar reflectivity factors for snow and ice particles. *J. Climate Appl. Meteor.,* **23,** 1258–1260, doi:10.1175/1520-0450(1984)023<1258:ERRFFS>2.0.CO;2.

Stevens, B., R. L. Walko, and W. R. Cotton, 1996: The spurious production of cloud-edge supersaturation by Eulerian models. *Mon. Wea. Rev.,* **124,** 1034–1041, doi:10.1175/1520-0493(1996)124<1034:TSPOCE>2.0.CO;2.

Straka, J. M., and E. R. Mansell, 2005: A bulk microphysics parameterization with multiple ice precipitation categories. *J. Appl. Meteor.,* **44,** 445–466, doi:10.1175/JAM2211.1.

Sulia, K., J. Y. Harrington, and H. Morrison, 2013: A method for adaptive habit prediction in bulk microphysical models. Part III: Applications and studies within a two-dimensional kinematic model. *J. Atmos. Sci.,* **70,** 3302–3320, doi:10.1175/JAS-D-12-0316.1.

Takahashi, T., 1976: Hail in an axisymmetric cloud model. *J. Atmos. Sci.,* **33,** 1579–1601, doi:10.1175/1520-0469(1976)033<1579:HIAACM>2.0.CO;2.

Thompson, G., R. M. Rasmussen, and K. Manning, 2004: Explicit forecasts of winter precipitation using an improved bulk microphysics scheme. Part I: Description and sensitivity analysis. *Mon. Wea. Rev.,* **132,** 519–542, doi:10.1175/1520-0493(2004)132<0519:EFOWPU>2.0.CO;2.

——, P. R. Field, R. M. Rasmussen, and W. D. Hall, 2008: Explicit forecasts of winter precipitation using an improved bulk microphysics scheme. Part II: Implementation of a new snow parameterization. *Mon. Wea. Rev.,* **136,** 5095–5115, doi:10.1175/2008MWR2387.1.

Van Weverberg, K., 2013: Impact of environmental instability on convective precipitation uncertainty associated with the nature of the rimed ice species in a bulk microphysics scheme. *Mon. Wea. Rev.,* **141,** 2841–2849, doi:10.1175/MWR-D-13-00036.1.

Verlinde, H., and W. R. Cotton, 1993: Fitting microphysical observations of nonsteady convective clouds to a numerical model: An application of the adjoint technique of data assimilation to a kinematic model. *Mon. Wea. Rev.,* **121,** 2776–2793, doi:10.1175/1520-0493(1993)121<2776:FMOONC>2.0.CO;2.

Walko, R. L., W. R. Cotton, M. P. Meyers, and J. Y. Harrington, 1995: New RAMS cloud microphysics. Part I: The one-moment scheme. *Atmos. Res.,* **38,** 29–62, doi:10.1016/0169-8095(94)00087-T.

Wang, H., W. C. Skamarock, and G. Feingold, 2009: Evaluation of scalar advection schemes in the Advanced Research WRF model using large-eddy simulations of aerosol-cloud interactions. *Mon. Wea. Rev.,* **137,** 2547–2558, doi:10.1175/2009MWR2820.1.

——, T. Auligne, and H. Morrison, 2012: Impact of microphysics scheme complexity on the propagation of initial perturbations. *Mon. Wea. Rev.,* **140,** 2287–2296, doi:10.1175/MWR-D-12-00005.1.

Weisman, M. L., and J. B. Klemp, 1982: The dependence of numerically simulated convective storms on vertical wind shear and buoyancy. *Mon. Wea. Rev.,* **110,** 504–520, doi:10.1175/1520-0493(1982)110<0504:TDONSC>2.0.CO;2.

——, and ——, 1984: The structure and classification of numerically simulated convective storms in directionally varying wind shears. *Mon. Wea. Rev.,* **112,** 2479–2498, doi:10.1175/1520-0493(1984)112<2479:TSACON>2.0.CO;2.

Zhang, F., N. Bei, R. Rotunno, C. Snyder, and C. C. Epifanio, 2007: Mesoscale predictability of moist baroclinic waves: Convection-permitting experiments and multistage error growth dynamics. *J. Atmos. Sci.,* **64,** 3579–3594, doi:10.1175/JAS4028.1.

Ziegler, C. L., 1985: Retrieval of thermal and microphysical variables in observed convective storms. Part I: Model development and preliminary testing. *J. Atmos. Sci.,* **42,** 1487–1509, doi:10.1175/1520-0469(1985)042<1487:ROTAMV>2.0.CO;2.